Erasmus+

PSRS

Erasmus Mundus Joint Master degree
Photonics for Security Reliability and Safety

Master in *Photonics for Security Reliability and Safety* (PSRS)

UNIVERSITÉ DE LYON | UNIVERSITÉ JEAN MONNET SAINT-ÉTIENNE | UNIVERSITY OF EASTERN FINLAND | UPEC UNIVERSITÉ PARIS-EST CRÉTEIL VAL DE MARNE Connaissance - Action | POLITECNICO DI TORINO

Graphene enhanced dielectric metasurface: towards close to perfect absorption.

Master Thesis Report

Presented by

Muhammad Muaz Iqbal

and defended at

University Jean Monnet, Saint-Etienne

August 22, 2023

Academic Supervisors: Ricciardi Carlo **Supervisors:** Prof. Polina Kuzhir **Co-Supervisor**: Dr Alexey Basharin	**Jury Committee:** **1**

Abstract

The main objective of this project is designing, fabricating and characterizing graphene-like film enhanced dielectric metasurface to approach close to perfect absorption at various incident angles. This thesis focuses on numerical simulation (COMSOL Multiphysics) of the dielectric metasurface coupled with conductive graphene-like film to optimize the structure (geometry of the metasurface and requirements to the conductive film) and experimental realization and testing close to perfect absorber due to interaction between fabricated layers. 3D printing fabricated an array of dielectric particles, supporting high, almost perfect absorption. We found that dielectric metamaterial coupled with graphene-like film could tune the multipole response, whereas conductive film supports lower absorption at a wide range of incident light. The combination of both of them as a sandwich structure gives rise to the possibilities for high, wide-band absorption.

The graphene-like film is 5-100 thicker than graphene monolayers, so the electromagnetic (EM) response can be easily characterized by the conventional techniques allowing the quantitative description of their properties. The absorption and transmission of the resultant structure were studied numerically, experimentally, and theoretically. Based on the theoretical predictions, we perform numerical simulations using COMSOL Multiphysics to see the electromagnetic response of dielectric particles. 3D voids structures were printed with different diameters, heights, and spacing between them. Graphene-like films were synthesized by pyrolysis at $800°C$ on a silicon dioxide SiO_2 substrate further used for dielectric metasurface printing. The experimental data acquired through THz time-domain spectroscopy for samples comprising voids with diameters ranging from 310 µm to 1240 µm and heights from 50 to 240 µm demonstrate their exceptional ability to absorb THz radiation. Optimized for the moment structure (Case 6) shows absorption 0.855 and transmission 0.145, in the broad frequency range from 0.1 to 1 Thz, making graphene-like film attractive for EM interference shields in airspace, electronic device, and communication applications.

Acknowledgement

First and foremost, in the name of **Allah**, the most merciful and the most gracious. I am thankful to Almighty Allah for such beautiful life and for granting me one of the most prestigious scholarships (EMJMD PSRS). I sincerely thank **Prof. Polina Kuzhir**, my supervisor, for her continuous support, direction, and mentorship throughout this project. Her knowledge, understanding, and support have been priceless to me, and I am incredibly grateful that she has been my guide throughout this academic journey.

I want to extend my heartfelt gratitude to **Dr Alexey Basharin** (co-supervisor) for his invaluable support and guidance throughout this research. His valuable insights, feedback, and constructive critiques have greatly enhanced my research experience and played a pivotal role in shaping this work.

I thank the University of Eastern Finland for providing me with the resources, environment, and opportunities to pursue my research. The knowledge and experiences I have gained here will serve me well in my future endeavours.

I sincerely thank the coordinators, my instructors, and particularly **Dr Nathalie DESTOUCHES**, **the EMJMD PSRS** Programme coordinator, for her prompt advice and assistance during the two-year journey.

I sincerely appreciate my parents and siblings' unwavering love, sacrifices, and belief in my capabilities. My strength is Their support, and I dedicate this work to them.

Finally, even though this work has my name, it represents the culmination of the individual efforts, encouragement, and faith of everyone listed above. I will always be thankful.

Joensuu, August 22th,2023

Muhammad Muaz Iqbal

Contents

Abstract i

Acknowledgement ii

List of Figures v

List of Tables vi

1 Introduction 1

1.1 Metamaterial 4

1.2 Carbon Allotropes 6

1.3 History of Graphene 8

1.4 Graphene - Properties 10

1.4.1 Electronic properties 10

1.4.2 Mechanical properties 10

1.4.3 Optical properties 11

1.4.4 Other properties 13

1.5 Potential Application of Graphene 13

2 Electromagnetic Modelling 17

2.1 Multipole expansion in electromagnetism 17

2.1.1 Maxwell Equations 17

2.2 An electromagnetic Multipole expansion 24

2.3 Theory 25

2.3.1 Anapole 29

2.3.2 Kerker Effect 32

2.3.3 Fano Resonance 34

3 Experimental Work 35

3.1 3D Printing (Phrozen Sonic Mini 8K) 35

3.1.1 Liquid Crystal Display 3D Printing 35

3.1.2 (Phrozen Sonic Mini 8K) 36

3.1.3 Printing Safety 37

3.1.4 Slicer Compatible & Printing flow work 37

3.1.5 Washing and Curing 38

3.2 Sample Fabrication 39
3.3 Terahertz Spectroscopy 40
4 Result and Discussion 43
4.1 Modelling result 43
5 Conclusion 54
Reference 57
List of Symbols, Operators and Special functions 66
Symbols Operators Special functions 66
Right and Permission 71

List of Figures

Figure 1 There are three forms of graphene. 2
Figure 2 Positive and negative refractive index 6
Figure 3 Various carbon allotropes 7
Figure 4 Andre Geim And Konstantin Novoselov, University of Manchester, UK 9
Figure 5 Applications for graphene in the industry are based on several manufacturing areas..... 14
Figure 6 (A) Optical microscope image of isolated single-layer graphene with 9m size for the first time by Geim and Novoselov [60]. Photographs of; (B) and (C) The largest monolayer graphene produced on copper reported so far (24'' by 300''). 15
Figure 7 Structure of a dynamic anapole[77]. 30
Figure 8 Radiation patterns of the electric (p), magnetic (m) and toroidal (T) dipoles[77]. 32
Figure 9 A schematic depiction of an LCD–digital light processing (DLP) 3D printer. 36
Figure 10 (1). Building plate (2). Resin Vat (3). LCD screen (4). Touch Panel (5). USB Port (6). Plastic Case (7). Z- axis 38
Figure 11 illustrates the process flow to synthesize NiPPF on a dielectric substrate (B), Resulting NiPPF. 40
Figure 12 Schematic of EM spectrum showing the position of THz band O.1 -10 THz..... 41
Figure 13 Schematic representation of the THz time-domain spectroscopy 42
Figure 14 (A) Simulation Image (voids) (B) Resulting plots of Voids (C) 3D printing coupled with NiPPF (D) Periodically arranged voids..... 43
Figure 15 Left side THz transmission of a 3D sample, right side 3D printed samples 46
Figure 16 Left side THz transmission of a 3D sample, right side 3D printed sample..... 47
Figure 17 Left side THz transmission of a 3D sample, right side 3D printed sample..... 48
Figure 18 NiPPF on top of a 3D sample 50
Figure 19 Left side THz transmission of a 3D sample, right side 3D printed sample..... 50
Figure 20 Left side THz transmission of a 3D sample, right side 3D printed sample..... 52
Figure 21 Left side THz transmission of a 3D sample, right side 3D printed sample..... 53

List of Tables

Table 1 Specification of Phrozen Sonic Mini 8K 37
Table 2 Different sample cases and their parameters 44
Table 3 Average Transmission (T) and Absorption (A) of case 1 (diameter 310 and height 50) μm 46
Table 4 Average Transmission (T) and Absorption (A) of case 2 (diameter 620 and height 100) µm 47
Table 5 Average Transmission (T) and Absorption (A) of case 3 (diameter 920 and height 150) µm 49
Table 6 Average Transmission (T) and Absorption (A) of case 4 (diameter 620 and height 100) µm 50
Table 7 Average Transmission (T) and Absorption (A) of case 5 (diameter 930 and height 150) µm 52
Table 8 Average Transmission (T) and Absorption (A) of case 6 (diameter 1240 and height 200) µm 53

1 Introduction

Professor Richard Feynman's 1959 lecture, "There is Plenty of Room at the Bottom," popularised "nanotechnology." "Nanotechnology" describes the interdisciplinary study of and work with materials on the nanometres scale (1–100 nm). Nanomaterials are important because of their ability to modify a material's properties by controlling its atomic structure. Given the wide range of allotropes that can be formed from the three bonds, carbon is capable of; carbon nanomaterials have been the subject of intensive study over the last three decades. Graphite, which is soft and brittle and made up entirely of sp2 hybridised bonds, is one of the recognised bulk allotropes of carbon; diamond, which is tough and made up entirely of sp3 hybridised bonds, is another; and amorphous carbon, which is non-crystalline and made up of both sp2 and sp3 hybridised bonds, is yet another. The level of accuracy with which nanomaterials may be evaluated has increased because of developments in microscope technology and other precision tools. Fullerenes (0D, Buckyballs), 2D-graphene, and carbon nanotubes - 1D are just a few of the carbon nanomaterials that have recently been explored thanks to technological advancements see figure 1.

Graphene has become a prominent material in the macro, micro, and nano-photonics industry since its discovery approximately twenty years ago [1]. It has received global recognition, including a Nobel Prize 2010 [2]. In contemporary times, ultrathin carbon thin films have been applied only in integrated optics environmental sciences, flexible electronics, water filtration, antireflective coatings, and textiles [3]. Considering the numerous advantageous characteristics of graphene, it possesses significant potential for utilization in both commercial and strategic contexts. Researchers from various countries actively research extensively to develop diverse graphene synthesis methods. Three important challenges exist in graphene production: scaling up for mass production, reducing costs, and ensuring high quality. Currently, there exist various techniques to produce graphene. These techniques can be broadly categorized into two main categories, one is known as top-down methods (such as exfoliation methods), and

another is bottom-up methods. The top-down approach involves using natural or synthetic graphite to extract individual graphene sheets through various ways, such as exfoliation techniques. According to the bottom-up process, graphene must be synthesized directly on a substrate utilizing a variety of methods, including epitaxial growth on silicon carbide (SiC), chemical synthesis, arc discharge, and chemical vapors deposition (CVD), plasma-enhanced chemical vapors deposition (PECVD), among others [4]. In a variety of applications, graphene's properties are significant. A graphene sheet's electrical and optical characteristics may suffer if it has grain boundaries, deficiencies, impurities, wrinkles, numerous domains, and structural problems.

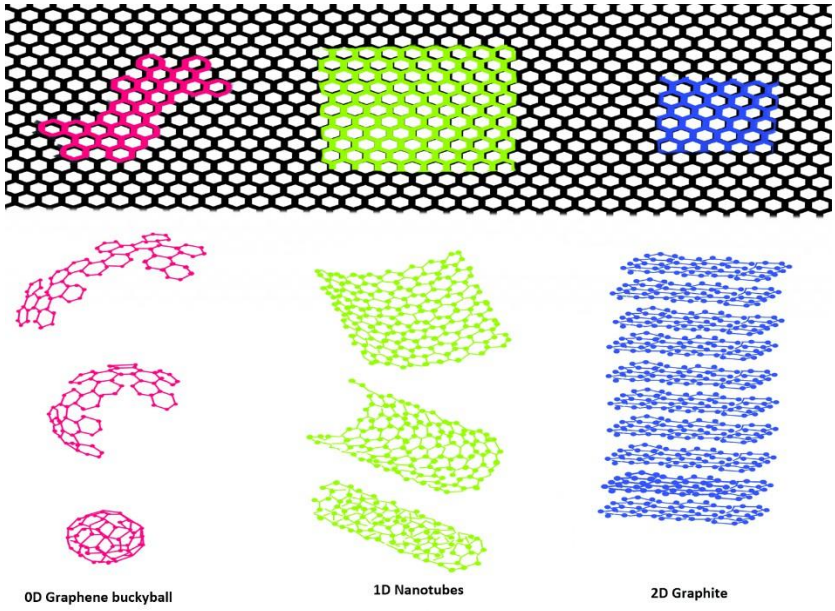

Figure 1 There are three forms of graphene.

Chemical vapor deposition presents challenges in generating thin graphene films of superior quality and single crystallinity, crucial for achieving exceptional electrical and thermal conductivity and remarkable optical transparency. CVD graphene has demonstrated its potential for utilization in a diverse range of compelling applications

encompassing touch layers, transistors, and sensors. Chemical vapor deposition has been associated with high production costs for an extended period. Consequently, CVD graphene has predominantly been utilized in research endeavours conducted by academic and research institutions. However, there has been a gradual decline in the price of CVD of monolayer graphene from 2015 to 2017. This cost reduction has paved the way for the emergence of commercial applications in the market. From 2015 to 2017, “Graphenea”, a prominent Spanish company specializing in the production of high-quality CVD graphene, experienced a notable decrease in prices for their graphene products [4]

Graphene is gaining attention as a highly promising material for developing stretchable and biocompatible electronic circuits. It is primarily attributed to its exceptional mechanical durability and flexibility, optical transparency, non-dispersive properties across a broad frequency spectrum, and compatibility with biological systems. However, it is important to note that not all applications require "ideal" graphene, which refers to a two-dimensional zero-gap semiconductor with exceptional tunability[5]. Thin graphitic films with adequate direct current (DC) and high-frequency conductivities can be a viable graphene alternative for various technological challenges[6].

Graphitic thin films can be broadly categorized into two main groups: (i) pyrolytic carbon films produced through the chemical vapor deposition (CVD) method and (ii) pyrolyzed polymer films PPF derived from the pyrolysis of carbon-rich precursor thin films.

In 1985, an alternative proposal was made to utilize pyrolyzed polymer films (PPF)[7]. The significant advantage of PPF is its low conductivity compared to metal[8]. Additionally, its chemical stability and robustness make it highly beneficial for a wide range of applications, including biological[9], electrochemical[10], and microelectromechanical applications[11]. Furthermore, compared to graphene, PPF exhibits an easier fabrication process compatible with conventional microelectronic platforms. Significantly, exposure to a high-energy electron beam causes alterations in

the chemical properties of the resist, rendering it insoluble in developers[12]. Consequently, this may impact the physical characteristics of the resulting graphitic film.

All-dielectric particles are the building blocks of metamaterials and metasurfaces due to lower dissipative losses in THz and optics and supporting both electric and magnetic Mie-resonances. However, the Q-factor of metamaterials is sufficiently diminishing as soon as the permittivity of particles is suppressed. In this work, we propose to use voids in an all-dielectric matrix with low permittivity instead of particles. The Mie-resonance modes are excited for voids less than wavelength. We use circular holes (voids) instead of disks and expect strong absorption of THz waves for the system of printed 3D metasurface with pyrolyzed photoresist film with a sacrificial Nickel layer (NiPPF). Based on the theoretical predictions, we perform numerical simulations using COMSOL Multiphysics to see the electromagnetic response of dielectric particles. 3D voids structures were printed with different diameters, heights, and spacing between them. Graphene-like films were synthesized by pyrolysis at $800°C$ on a silicon dioxide SiO_2 substrate further used for dielectric metasurface printing. The experimental data acquired through THz time-domain spectroscopy for samples comprising voids with diameters ranging from 310 µm to 1240 µm and heights from 50 to 240 µm demonstrate their exceptional ability to absorb THz radiation.

1.1 Metamaterial

Metamaterials are artificially engineered materials with unique properties not found in naturally occurring materials[13]. It is an array of periodically arranged meta-atoms [14]. The term "metamaterial" was first used by R.W. Walser, with the prefix "meta" denoting a state beyond the natural state. Metamaterials exhibit distinct electromagnetic radiation responses compared to raw materials[15]. The origins of metamaterials can be traced back to 1968 when V. G. Veselago postulated that dielectric permittivity and permeability could exhibit negative values [16]. At the outset, these two were consistently regarded as positive [13]. This hypothesis anticipated extraordinary material

features, such as perfect lensing and a negative refractive index [16]. Still, his work went undetected since it wasn't backed up by experimental evidence because there weren't any materials with negative refraction at the time[17]. In 2000, J.B. Pendry introduced the concept of theoretically perfect lenses after a significant period of research and development. In the same year, D. R. Smith also demonstrated the first material with a negative refractive index [18]. Several metamaterials have been constructed since then [19].

The energy band determines the characteristics of normal materials, whereas the geometry of meta-atoms determines the properties of metamaterials. Metamaterials can manipulate various forms of physical waves, particularly electromagnetic waves [13]. Metamaterials can function across the entire electromagnetic spectrum, ranging from radio waves to the visible spectrum. Metals can be classified as near-perfect absorbers, indicating their inability to transmit or reflect incoming electromagnetic waves [20]. The significant absorption of electromagnetic radiation is noteworthy due to its exceptional optical and electromagnetic characteristics[21]. It is possible to add graphene into a metamaterial device to increase its absorption capabilities further. Graphene nano-disks, graphene rings, and graphene sheets are all examples of different types of metamaterial absorbers based on graphene [22].

The equation that provides the refractive index of the material is as follows:

$$n = \sqrt{\varepsilon\mu}$$

The symbols Ɛ and μ represent the permittivity and permeability of the material, respectively. Figure 2 depicts the schematic diagram of the negative and positive refractive index. This is a typical illustration of light manipulation, whereby natural materials typically refract in the opposite direction. The graph illustrates that the refraction of light varies depending on whether the refractive index is positive or negative. In the event of a negative refractive index, the values of both permeability and permittivity will exhibit negativity [18].

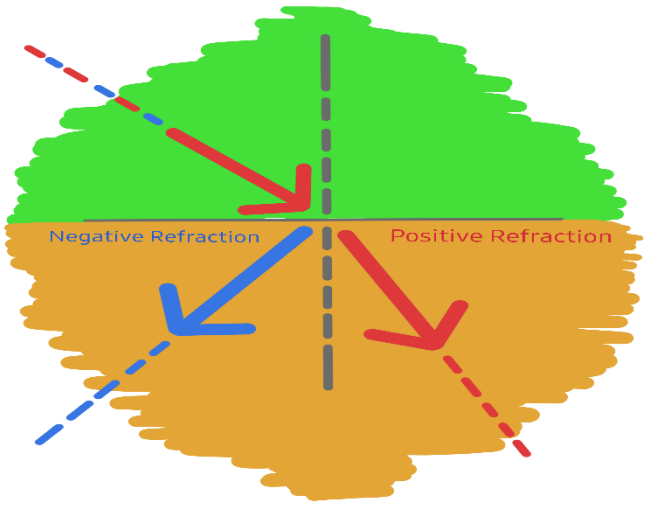

Figure 2 Positive and negative refractive index

Metamaterials are recognized for their ability to manipulate light propagation and are highly advantageous for operation within the terahertz (THz) frequency range [23]. The terahertz range spans from 0.1 to 10 THz, which aligns with the wavelength range of 3 mm-30 µm, commonly called the terahertz gap. Devices that operate in the (THz) range have various applications in fields such as medical imaging, communication, chemical identification, sensors, and astronomy [24]. Furthermore, the primary focus is on attaining adjustability of metamaterials within the terahertz frequency range [25].

1.2 Carbon Allotropes

The Earth's crust contains a substantial amount of carbon C. It has the atomic number 6 and electron configuration [He]2s2 2p2. Additionally, it is worth noting that oxygen is a highly abundant element in the human body by mass, accounting for approximately 18.5%. In addition, carbon is ranked as the fourth most prevalent element in the universe in terms of the group, preceded by hydrogen, helium, and oxygen. The term "carbon"

has its roots in the Latin word "carbon," which was employed by the ancient Romans to denote charcoal or ember. In present-day society, the term "carbon" holds a wide range of significance[26]. This commonly encountered substance exhibits a distinct and noteworthy functionality in chemistry and materials research. Carbon shows a diverse array of applications, spanning from pharmaceuticals to artificial materials. Specific industrial applications include producing oil and gas, food, medications, water purification, hydrometallurgy, gold recovery, and the commonly used carbon-in-pulp process [27].

Carbon is characterized by its capacity to generate diverse allotropes and its aptitude to bond with other chemical elements. The allotropes of carbon can be categorized based on their spatial dimensionality. The fullerenes are classified as zero-dimensional, while carbon nanotubes are considered one-dimensional. Graphite and diamond are categorized as three-dimensional, whereas graphene is classified as two-dimensional. The fundamental distinction between two-dimensional (2D) and three-dimensional (3D) structures is determined by the number of atomic layers present.

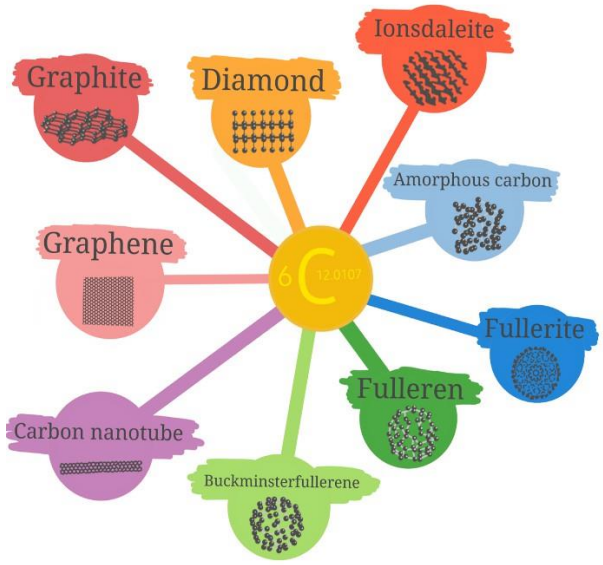

Figure 3 Various carbon allotropes

For example, Two-dimensional (2D) carbon is a single atomic crystal layer, whereas 3D graphite has hundreds of graphene layers [28]. In earlier times, elemental carbon was recognised to occur exclusively in two natural allotropes, specifically diamond and graphite. Both allotropes demonstrate distinct thermal and electrical properties. In 1985, a group of researchers led by Kroto made a significant discovery regarding a previously unknown variation of carbon, which they named fullerenes [29]. After this considerable advancement, a new era of synthetic carbon allotropes commenced with the discovery of carbon nanotubes in 1991 [30] and the 2004 rediscovery of graphene. There are more than nine carbon alterations in figure 3.

1.3 History of Graphene

The optimal configuration of graphene consists exclusively of a planar lattice structure composed of hexagonal cells. Sir Benjamin Collins Brodie was the first to describe the finely layered structure of thermally reduced graphite oxide in 1859 when graphene's history began. In 1947, P.R. Wallace postulated the potential existence of graphene on a theoretical basis.

The term "graphene" was initially introduced in 1987 to refer to the layers of graphite that were intercalated with different compounds. In 1948, the initial electron microscopy led to the discovery of images depicting multiple layers of graphite. After that, Ruess and Vogt observed single graphene layers [31]. Afterwards, the attempt to isolate graphene commenced. In 2004, Professors Andre Geim and Constantine Novoselov from Manchester University successfully separated a single atomic layer of carbon (graphene) from graphite. It was observed that specific flakes varied in thickness compared to others. Through the iterative separation of graphite fragments, they create flakes that consist of a single atom layer. The participants used a technique involving manipulating graphite cubes and using Scotch tape to remove flakes of graphite.

Figure 4 Andre Geim And Konstantin Novoselov, University of Manchester, UK

The process was repeated multiple times to obtain thinner graphite flakes by separating them into increasingly thinner layers until a thickness of only one atom was achieved. It is not feasible to reduce the thickness of the materials beyond one atom; hence this substance represents the closest approximation to a two-dimensional system that can be achieved physically. Geim and Novoselov are credited with discovering graphene, which Wallace first proposed. The "scotch tape" method has proven to be a straightforward and efficient approach, leading to a rapid expansion of its application in the field of Science. Numerous research institutions worldwide employ this technique for investigating graphene due to its cost-effectiveness and minimal equipment requirements (Novoselov KS, 2004). Andre Geim and Konstantin Novoselov were the 24th and 25th Nobel Laureates in the University's history when they were awarded the Nobel Prize in Physics in 2010 for their major contributions to the discipline [31].

1.4 Graphene - Properties

1.4.1 Electronic properties

The main driving force behind the research on graphene was its unique two-dimensional structure and symmetrical properties, which lead to its charge carriers displaying behaviour similar to that of massless relativistic particles [32]. It is classified as a no-band gap semiconductor because its valence and conduction bands intersect at corners of the Brillouin zone. The material shows an ambipolar electric field effect, allowing for adjustable concentrations of electrons and holes up to 1013 cm^{-2}. Additionally, it boasts charge carrier mobilities (μ) of up to 15000 $cm^2/(Vs)$ at room temperature [33]. An observation was made of ballistic transport with a mobility (μ) exceeding 2×10^5 $cm^2/(Vs)$ at an electron density of approximately 2×10^{11} cm^{-2}, upon minimising the extrinsic scattering in suspended single-layer graphene (SLG) [34]. High values of μ have been reported in recent times. Graphene nested between two hexagonal boron-nitride crystals has recorded a value of 2.5 × 105 cm2/(Vs) at room temperature[35] with a mean free path of µm scale. Epitaxially grown graphene on silicon carbide has recorded a value of ~6 × 106 cm2/(Vs) at 4 K [36]. The unique electronic properties of graphene make it a highly promising contender for future electronic devices [37]. Since graphene cannot be used in conventional field-effect transistors (FET) due to its zero-band gap, researchers are focusing on high-frequency applications in the communications domain.

1.4.2 Mechanical properties

Frank et al.'s initial research on graphene's mechanical characteristics appeared in 2007 [38]. The spring constant of FLG (few-layer graphene) with a thickness of less than five layers was determined by measuring force-displacement using an AFM (atomic force microscope) tip. The Young's modulus of graphene was determined to be 0.5 TPa, while the spring constant was found to vary between 1 and 5 N/m. Lee et al. conducted a comparable atomic force microscopy (AFM) nanoindentation method on a sin (SLG)

sheet that was suspended over a hole with a diameter of 1 – 1.5 μm in a silicon substrate [39]. The AFM tip applied indentation on the graphene sheet until it reached a point of rupture, allowing for the subsequent determination of Young's modulus based on the force-depth curve. The strength of Young's modulus and monolayer graphene was estimated to be approximately 1 TPa and 130 GPa, respectively. The remarkable characteristics of this material can be defined as the strength of its in-plane covalent sp2 bond, rendering it the most resilient substance currently identified. Graphene has been demonstrated to exhibit elastic stretching capabilities of up to 20%[39]. Liu et al. employed density functional theory to estimate Young's modulus and strength of single-layer graphene to be approximately 1.05 TPa and 107-121 GPa, respectively. These values remarkably concurred with the experimentally determined values [40]. Other studies have also yielded comparable results for Young's-modulus of graphene using alternative techniques, including resonators and Raman spectroscopy [41], [42]. Furthermore, it has been observed that graphene exhibits impermeability to various gases, including helium [43]. When individual gas molecules were adsorbed on the graphene surface, resistivity values were seen, mostly due to changes in Fermi levels, making it a very sensitive gas detector [44].

1.4.3 Optical properties

The study by Novoselov et al. 2004 provided evidence of the observable alterations in reflection between graphene and the substrate when graphene is applied to an interferometer. In 2007, a published article reported a method for identifying and quantifying the number of graphene layers using a SiO_2 interferometer. This approach relied on the sensitivity of optical reflection measurements [45]. The optical response of graphene exhibits an extraordinary level of efficacy for a monoatomic layer, with approximately 2% absorption. Consequently, the material absorbs and reflects a minimal fraction of incident light, resulting in a nearly transparent appearance of the graphene layer. The number of graphene layers present influences the absorbance of a material. This relationship is determined by multiplying the fine-structure constant, denoted as

$\alpha = \frac{e^2}{\hbar c^2}$, by the number of graphene layers, represented as $\pi\alpha$. When the number of layers is increased from 1 to 10, its reflectance rises from 0.1 to roughly 2% [46]. The optical properties of graphene render it highly advantageous for implementation in optoelectronic and photonic devices.

Additionally, graphene is useful in various applications, such as photodetectors, optical limiters, smart windows, and saturable absorbers. Graphene and other carbon allotropes exhibit exceptional nonlinear optical (NIO) properties. These properties are crucial in developing and producing optoelectronic and photonic devices at the nanoscale.

Different nano-carbons demonstrate a wide range of NIO properties. For instance, carbon black suspensions exhibit a significant thermally-induced NLS (nonlinear scattering) effect, resulting in optical limit (OL) when it is exposed to a strong nanosecond laser pulse [47]; Fullerenes demonstrate a substantial third-order optical nonlinearity and reverse saturable absorption (RSA) within specific wavelength bands [48]; Carbon nanotubes (CNTs) display ultrafast second- and third-order nonlinearities as well as saturable absorption (SA) in the near-infrared (NIR) region [49]; Lastly, graphene's exhibit an ultra-fast relaxation time of charge carriers and an ultra-broad-band resonance nonlinear optical (NIO) response [50]. The utilization of graphene in advancing practical nano-carbon devices is constrained by its challenge to maintain stability in various organic solvents [51]. It is crucial to emphasize the importance of designing and synthesizing a solution-processed organic/polymeric material based on graphene. Optical limiting is a significant nonlinear optical (NLO) phenomenon important in safeguarding sensitive optical instruments against high-intensity laser beams. Its application is particularly relevant in protecting the human eye [52].

1.4.4 Other properties

Graphene exhibits unique thermal properties, with the intrinsic thermal conductivity of single-layer graphene ranging between 3000-5000 W/(mK)[53]. It has been observed that the thermal conductivity decreases as the number of layers increases, reaching a value of 1300 W/(mK) for four layers, which approaches the thermal conductivity of bulk graphite [54]. A high level of thermal conductivity facilitates efficient heat dissipation, making it a highly suitable option for thermal management [55].

The SLG exhibits a light absorption rate of 2.3%, with a negligible reflectance level of less than 0.1% [46]. The remarkable integration of mechanical flexibility, strength and elasticity, and optical and electronic properties render graphene ideal for applications in flexible electronics and touchscreen devices [56].

Furthermore, it has been theoretically estimated that the surface area of (SLG) is approximately 2600 m2/g. Experimental studies have reported a range of surface area values for few-layer graphene (FLG), ranging from 270 to 1550 m2/g [57]. The high surface area has proven advantageous in various fields, such as nanocomposites, through surface modification. This technique enhances the interaction between the matrix and graphene at the interfacial level [41].

1.5 Potential Application of Graphene

Graphene is a highly versatile and resilient material with exceptional application performance. Furthermore, graphene has established itself as a highly valuable material with the potential to enhance or redefine numerous applications within the current paradigm. The technology has garnered significant interest and adoption across various industries, including synthesis and processing, construction, energy storage, telecommunications, composites, biomedicine, automotive sectors, and energy generation.

According to the pie diagram provided in figure 5, it is evident that a substantial portion of graphene is utilized in the electronics and energy storage and aerospace sectors. Graphene is pivotal in driving advancements in modern technology applications [58].

Graphene's high carrier mobilities, approximately 40 times greater than the typical electron mobility for silicon, contribute to electronic application attractiveness. Additionally, graphene exhibits a high current-carrying capability. These advantageous characteristics position graphene as a relevant material for utilization in electronic devices. Furthermore, due to its significant thermal conductivity, which plays a crucial role in the shrinking of electronic devices as circuit density increases, graphene effectively maintains device temperature by efficiently dissipating heat. However, achieving large-scale graphene growth is imperative and essential to further harness and capitalize on its inherent properties.

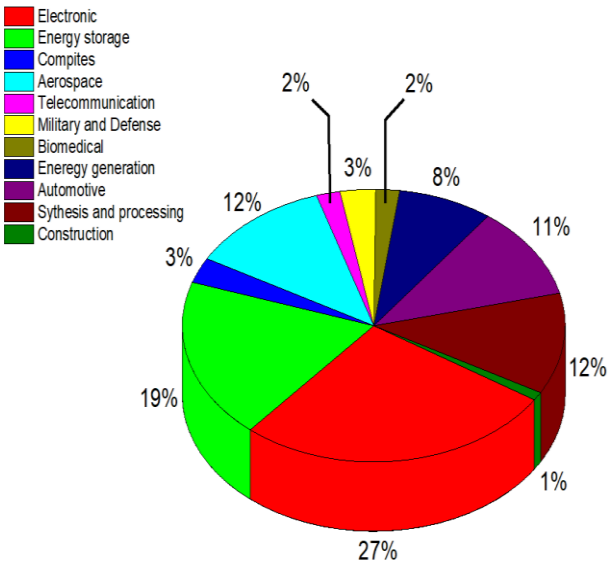

Figure 5 Applications for graphene in the industry are based on several manufacturing areas.

Figure 6 illustrates the progressive advancement in the synthesis of graphene, showcasing the transition from micrometre-scale to inch-scale dimensions. Following the groundbreaking work of Geim and Novoselov [59], the isolation of monolayer graphene with a size of only µm was achieved. Subsequently, a significant advancement was made in producing single-layer graphene, with a size of 30 inches, utilizing the (CVD) method. The largest reported monolayered graphene measures 24 inches by 300 inches and was grown on copper using the (CVD) process. The utilization of graphene in touch panels [56] was made possible due to its exceptional properties, such as high transparency, flexibility, and conductivity.

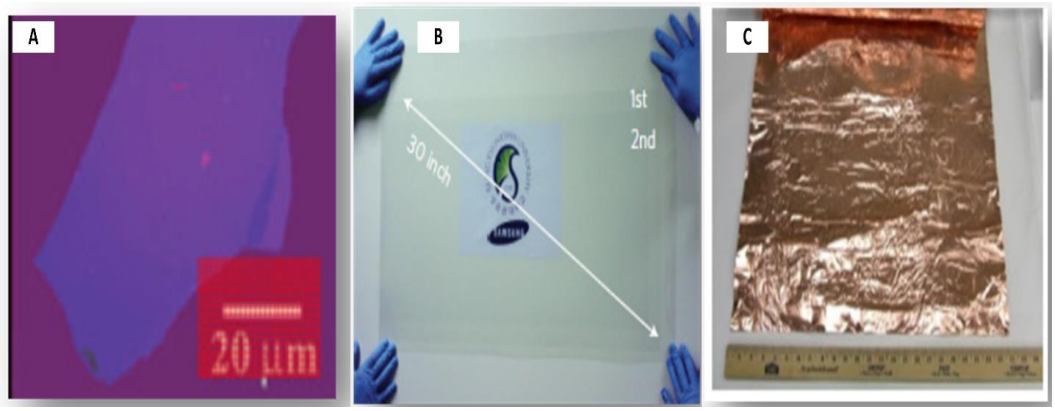

Figure 6 (A) Optical microscope image of isolated single-layer graphene with 9m size for the first time by Geim and Novoselov [60]. Photographs of; (B) and (C) The largest monolayer graphene produced on copper reported so far (24'' by 300'').

Graphene exhibits significant potential as a material for gas sensors, extending beyond its applications in electronics. The electronic properties of graphene are measurably influenced by the deposition of gas molecules, allowing for the detection of gases [60].

Graphene has the potential to be utilized as a support material in the field of catalysis owing to its substantial surface area. Additionally, it can serve as electrode material in various electrochemical applications, including batteries and supercapacitors. The layered structure of graphene acts as a protective barrier, preventing the aggregation of nanoparticles within the catalyst or electrode material. Using chemically derived

graphene (CDG) or reduced graphene oxide (RGO) materials as anodes or cathodes in lithium-ion battery technology has contributed to advancements in the field. This is primarily due to the significant surface-to-volume ratio and excellent conductivity properties exhibited by graphene. The generation of nanopores and defects in the carbon-doped graphene (CDG) via chemical synthesis facilitates the creation of active sites for lithium insertion, which play a vital role in lithium battery technology.

2 Electromagnetic Modelling

2.1 Multipole expansion in electromagnetism

This section will overview electromagnetism concerning electromagnetic (EM) multipole moments. The text highlights several significant points about metamaterials. In the next section, we will explain the multipole moments of molecules in the microscopic Maxwell equations and their impact with the macroscopic solutions.

2.1.1 Maxwell Equations

The Maxwell equations elucidate EM fields made by electrically charged particles in a vacuum on a microscopic scale. In SI units, the formulae can be written as:

$$\nabla \cdot \mathbf{e}(\mathbf{r}, t)\& = \frac{\rho_m(\mathbf{r}, t)}{\epsilon_0} \tag{1}$$

$$\nabla \cdot \mathbf{b}(\mathbf{r}, t)\& = 0 \tag{2}$$

$$\nabla \times \mathbf{e}(\mathbf{r}, t)\& = -\frac{d\mathbf{b}(\mathbf{r}, t)}{dt} \tag{3}$$

$$\nabla \times \mathbf{b}(\mathbf{r}, t)\& = \frac{1}{c^2}\frac{d\mathbf{b}(\mathbf{r}, t)}{dt} + \mu_0 \mathbf{j}_m(\mathbf{r}, t) \tag{4}$$

The characteristics of the microscopic **e, b** electric field, and magnetic density, which are produced by microscopic $\boldsymbol{\rho_m}$ $\mathbf{j}_m$ charge and current density. Within a three-dimensional space, These four quantities depend on the position. $(\mathbf{r})$ and time (t). The $c^2 = \sqrt{\epsilon_0 \mu_0}$ represent the speed of light c^2, the magnetic permeability μ_0, and electric permittivity ϵ_0 in a vacuum.

It can be observed that matter is composed of discrete charged particles. The microscopic quantities exhibit non-smooth variations with respect to position. Therefore, they are typically subjected to spatial averaging. The averaging process is conducted over volumes that are sufficiently large to ensure that the averaged quantities, $< \rho_m >$ and $< \mathbf{j}_m >$ exhibit smooth variations in both space and time. However, it is important to note that volume dimensions should be significantly lower than the length scale of spatial variations of $< \mathbf{b} >$ and $< \mathbf{e} >$, which are the primary focus of our interest. Suppose one is interested in studying electromagnetic wave propagation within a medium. In that case, it is important to ensure that the lengths of the averaging volume are significantly smaller than the wavelength.

It is possible to perceive matter as comprising two distinct categories of electrically charged particles. Initially, it is important to note the existence of elementary particles that exhibit a cohesive arrangement within different clusters. The entities referred to as clusters are commonly known as molecules. Secondly, the medium contains unbound conduction electrons not confined to a specific molecule. The particle type mentioned above is restricted to volumes significantly smaller than the volume used for averaging. Consequently, it is possible to perceive each molecule as a point particle. Molecules are given multipole moments to describe the current distributions and internal charge distributions inside them.

Consider a specific molecule denoted by the variable l th, where the center of mass of this molecule is located $\mathbf{r}_l$. $\mathbf{v}_l$ denoted as the velocity of the center mass. The molecule potentially possesses an overall electric charge.

$$q_l = \sum_{j(l)} q_j \tag{5}$$

electric dipole moment

$$\mathbf{P}_l = \sum_{j(l)} q_j(\mathbf{r}_j - \mathbf{r}_l) \tag{6}$$

electric quadrupole moment

$$\overleftrightarrow{\mathrm{q}}_l = \frac{1}{2}\sum_{j(l)} q_j(\mathbf{r}_j - \mathbf{r}_l)(\mathbf{r}_j - \mathbf{r}_l) \tag{7}$$

And the magnetic dipole moment

$$\mathbf{m}_l = \frac{1}{2}\sum_{j(l)} q_j(\mathbf{r}_j - \mathbf{r}_l) \times (\mathbf{v}_j - \mathbf{v}_l) \tag{8}$$

If we add the values of all the molecule's fundamental particles, j. $\mathbf{r}_j$, $\mathbf{v}_j$ is the position and velocity, and q_j is the charge of the j^{th} particle in Eqs. {5} – {8}. For simplicity, higher-order electric and magnetic moments are less important and may be ignored. Eq {8} considers the molecule's orbital magnetic moment since it is a classical equation. The magnetic dipole moment also incorporates the spins of the fundamental particles. It is often necessary to compute the real multi-pole moments of individual molecules using quantum mechanics[61].

The unbound conduction electrons will be the subject of our next analysis. These particles' associated charge and current densities are regarded as separate entities. The process involves incorporating $(\rho_{c.e.})$ and $(j_{c.e.})$. Where $(\rho_{c.e.})$ and $(j_{c.e.})$ are the conduction electron charge and current density into the averages of the corresponding molecular quantities. The overall $\rho = <\rho_m>$ and $\boldsymbol{J} =<\mathbf{j}_m>$, become zero in a stationary medium where molecules may be considered to have zero velocity.

$$\rho(\mathbf{r},t) = \rho_F(\mathbf{r},t) - \nabla\cdot\mathbf{P}(\mathbf{r},t) + \nabla\cdot(\nabla\cdot\overleftrightarrow{\mathbf{Q}}(\mathbf{r},t)), \tag{9}$$

$$\mathbf{J}(\mathbf{r},t) = \mathbf{J}_F(\mathbf{r},t) + \frac{d}{dt}(\mathbf{P}(\mathbf{r},t) - \nabla\cdot\overleftrightarrow{\mathbf{Q}}(\mathbf{r},t)) + \nabla\times\mathbf{M}(\mathbf{r},t), \tag{10}$$

The symbols used in the equation are as follows: ρ_F, $\mathbf{J}_F$, $\mathbf{P}$, $\mathbf{M}$ and $\overleftrightarrow{\mathbf{Q}}$ represents the free charge density, the electric polarization, current density, the magnetization, and quadrupole moment density. The medium obtained the following five quantities, representing macroscopic features of the media [61].

$$\rho_F(\mathbf{r},t)\& = <\sum_l q_l(t)\delta(\mathbf{r}-\mathbf{r}_l)> + \rho_{\text{c.e.}}(\mathbf{r},t), \tag{11}$$

$$\mathbf{J}_F(\mathbf{r},t)\& = \mathbf{J}_{\text{c.e.}}(\mathbf{r},t), \tag{12}$$

$$\mathbf{P}(\mathbf{r},t)\& = <\sum_l \mathbf{p}_l(t)\delta(\mathbf{r}-\mathbf{r}_l)>, \tag{13}$$

$$\mathbf{M}(\mathbf{r},t)\& = <\sum_l \mathbf{m}_l(t)\delta(\mathbf{r}-\mathbf{r}_l)>, \tag{14}$$

$$\overleftrightarrow{\mathbf{Q}}(\mathbf{r},t)\& = <\sum_l \overleftrightarrow{\mathbf{q}}_{l_l}(t)\delta(\mathbf{r}-\mathbf{r}_l)> \tag{15}$$

Every molecule in the medium is included in the summation. The first part in Eq. (11) represents the positively charged ions in a metallic environment, while another term represents the negatively charged group of conduction electrons. It is crucial to note that only conduction electrons contribute to $\mathbf{J}_F$, while ions and conduction electrons both

contribute to the characteristic known as ρ_F,. The ions are distinguished because it is considered that they are stationary in space.

In most natural materials, the value of $\overleftrightarrow{\mathbf{Q}}$ can be disregarded in Eqs {9} and {10}. This is because, in general, the impact of $\overleftrightarrow{\mathbf{Q}}$ on EM interaction effects is typically less than of electric polarization [62]. Furthermore, it has been observed that at optical frequencies, the impact of magnetization on ρ and current density is significantly insignificant when correlated to the influence of polarization [63]. Various EM processes also need higher-order moments, such as magnetic quadrupole and electric octupole moments [64].

Equations {1} through {4} will be averaged, and their expressions will be replaced with those from equations {9} and {10}. Consequently, the macroscopic Maxwell equations are derived.

$$\epsilon_0 \nabla \cdot \mathbf{E}(\mathbf{r},t) = \rho_F(\mathbf{r},t) - \nabla \cdot \mathbf{P}(\mathbf{r},t) + \nabla \cdot \left(\nabla \cdot \overleftrightarrow{\mathbf{Q}}(\mathbf{r},t) \right) \tag{16}$$

$$\nabla \cdot \mathbf{B}(\mathbf{r},t)\& = 0, \tag{17}$$

$$\nabla \times \mathbf{E}(\mathbf{r},t)\& = -\frac{d\mathbf{B}(\mathbf{r},t)}{dt}, \tag{18}$$

$$\begin{aligned} \nabla \times \mathbf{B}(\mathbf{r},t)\& = \mu_0 \frac{d}{dt}\left(\epsilon_0 \mathbf{E}(\mathbf{r},t) + \mathbf{P}(\mathbf{r},t) - \nabla \cdot \overleftrightarrow{\mathbf{Q}}(\mathbf{r},t) \right) \\ + \mu_0 (\mathbf{J}_F(\mathbf{r},t) + \nabla \times \mathbf{M}(\mathbf{r},t)) \end{aligned} \tag{19}$$

In this context, the symbols $\mathbf{E}$ and $\mathbf{B}$ represent the macroscopic magnetic and electric field flux density. Eqs {16}-{19} delineate the connections between the macroscopic fields and the macroscopic sources, denoted as ρ_F , $\mathbf{J}_F$, $\mathbf{M}$, $\mathbf{P}$, and $\overleftrightarrow{\mathbf{Q}}$. By applying the

divergence operator to Eq. {19} and utilizing Eq. {16}, the resulting expression corresponds to the continuity equation.

$$\frac{d\rho_F(\mathbf{r},t)}{dt} + \nabla \cdot \mathbf{J}_F(\mathbf{r},t) = 0 \tag{20}$$

By knowing $\mathbf{J}_F$, one can determine ρ_F.

The variables $\mathbf{E}$, $\mathbf{B}$, $\mathbf{P}$, $\overleftrightarrow{\mathbf{Q}}$, $\mathbf{M}$, ρ_F, and $\mathbf{J}_F$ in Eqs {16} - {19} to exhibit a sinusoidal temporal fluctuation with an angular frequency ω. In this scenario, it is possible to express the electric field in the following format:

$$\mathbf{E}(\mathbf{r},t) = \mathrm{Re}\left\{\mathbf{E}(\mathbf{r})e^{-i\omega t}\right\} \tag{21}$$

This defines the electric field's complex amplitude, E(r). The complex amplitudes of $\overleftrightarrow{\mathbf{Q}}$, $\mathbf{M}$ $\mathbf{E}$, $\mathbf{B}$, $\mathbf{P}$, ρ_F, and $\mathbf{J}_F$ are defined by analogous equations. In Eq. {20}, the continuity equation for time-harmonic fields has the following form.

$$i\omega\rho_F(\mathbf{r}) = \nabla \cdot \mathbf{J}_F(\mathbf{r}) \tag{22}$$

This principle also applies to the complex amplitudes of ρ and $\mathbf{J}$. The Maxwell equations are expressed as stated in reference [65].

$$\nabla \cdot \mathbf{D}(\mathbf{r})\& = 0 \tag{23}$$

$$\nabla \cdot \mathbf{B}(\mathbf{r})\& = 0 \tag{24}$$

$$\nabla \times \mathbf{E}(\mathbf{r})\& = i\omega \mathbf{B}(\mathbf{r}) \tag{25}$$

$$\nabla \times \mathbf{H}(\mathbf{r})\& = -i\omega \mathbf{D}(\mathbf{r}), \tag{26}$$

Where we've defined the electric displacement's complex value as

$$\mathbf{D}(\mathbf{r}) = \epsilon_0 \mathbf{E}(\mathbf{r}) + \mathbf{P}(\mathbf{r}) - \nabla \cdot \overleftrightarrow{\mathbf{Q}}(\mathbf{r}) + \frac{i}{\omega}\mathbf{J}_F(\mathbf{r}), \tag{27}$$

The complex amplitude of the magnetic field

$$\mathbf{H}(\mathbf{r}) = \frac{1}{\mu_0}\mathbf{B}(\mathbf{r}) - \mathbf{M}(\mathbf{r}). \tag{28}$$

Typically, the fields do not exhibit harmonic behaviour over time. If the sources $\mathbf{J}_F$, $\mathbf{P}$, $\overleftrightarrow{\mathbf{Q}}$, and $\mathbf{M}$, exhibit a linear relationship with the fields $\mathbf{E}$ and $\mathbf{B}$, it is possible to express these fields as integrals of the real part of $\mathrm{Re}\left\{\mathbf{E}(\mathbf{r})e^{-i\omega t}\right\}$and $\mathrm{Re}\left\{\mathbf{B}(\mathbf{r})e^{-i\omega t}\right\}$) over the frequency range ω. The eqs {23} – {26} can be applied to the integrand for each value of ω individually.

Thus far, we have examined EM fields within a molecule medium. The macroscopic properties of the medium are determined by the microscopic molecular moments and currents, as described by eqs {11} – {15}. The microscopic properties, which can be accurately determined using quantum mechanics QM, exhibit limitations transferred to the macroscopic properties through averaging. At optical frequencies, it is uncommon to encounter natural materials with a comparable value of $\mathbf{M}$ to $\mathbf{P}$. The limitations can be effectively addressed through the development and implementation of metamaterials.

The concept of metamaterials involves the intentional structuring of matter at a significantly smaller length scale than the expected spatial variations of electric $\mathbf{E}$ and magnetic fields $\mathbf{B}$. This enables applying a secondary spatial averaging process to eqs {23} – {26}. The method of structuring can lead to EM excitation of circulating electric currents. These currents, when averaged, give rise to an $\mathbf{M}$ in the revised macroscopic Maxwell Eqs. The construction of metamaterials that exhibit a $\mathbf{M}$ magnetic response at optical frequencies is crucial to study in metamaterials research.

2.2 An electromagnetic Multipole expansion

The utilization of multipole expansion is the fundamental technique in the examination of interactions between matter and light. A limited set of numerical values briefly represents the complete characterization of the radiation emitted by and interaction with electromagnetic fields of a specific charge-density distribution. The multipole moments are associated with the source. The set of numbers obtained from this process is commonly referred to as the multipolar moments. The items are categorized based on their respective order[66]. The first term, the monopole moment, corresponds to the 0th order. Subsequently, the second term, the dipole moment, corresponds to the 1st order. The third term, the quadrupole moment, corresponds to the 2nd order. Lastly, the fourth term, also referred to as the quadrupole moment, corresponds to the 3rd order. The phenomenon of increase is commonly referred to as the octupole moment. Following the limitations of Greek numeral prefixes, it is customary to designate higher-order terms by appending "-pole" to the pole number. For example, there are 32 poles, also known as dotriacontapols or triacontadepols, and 64 poles, occasionally referred to as tetrahexacontapols or hexacontatetrapols. Multipole moments generally encompass a term involving a power (or reciprocal power) of the distance from the origin and an angular dependency. The multipole expansion offers a reliable depiction of the potential. It typically exhibits convergence under two conditions: (1) When the source (e.g., charge) is concentrated in the region of the origin, and (2) when the point where the potential is observed is situated at a considerable distance from the origin. Alternatively, option (2)

involves the scenario where the source is situated considerably from the origin, while the potential is measured near the origin. The series expansion coefficients are called external or multipole moments in the initial scenario. Conversely, in the second scenario, they are denoted as internal multipole moments[67].

Every multipolar moment is intricately linked to its respective multipolar field. The significance of these moments arises from the fact that they fully describe the emission of electromagnetic fields by a charge-current distribution and the interaction of external fields with it. The multipolar decomposition is relevant to scientific disciplines studying interactions between material systems and electromagnetic fields. The study of multipole moments of nuclei in particle physics offers valuable insights into the internal charge distribution within the nucleus. In chemistry, a molecule's dipole and quadrupolar polarizabilities play a significant role in determining most of its properties. The multipole expansion is a widely employed technique in electrical engineering to assess the radiation characteristics of antennas [60] quantitatively.

In modern nano-photonics, multipolar interference is crucial for developing innovative optical devices, such as metasurfaces exhibiting exceptional functionalities. Nano-photonics is a field that focuses on the control and manipulation of light at the nanoscale. The multipole expansion offers valuable insights into various optical phenomena, including Fano resonances[68], electromagnetically-induced-transparency[69], directional light emission[70] manipulation and control of spontaneous emission[71], perfect absorption of light [20], electromagnetic cloaking[72], and the generation of optical forces (pulling, pushing, and lateral) [73]. An external field causes the particles to experience displacement or generate conductive currents in each instance. The induced currents serve as the origin of the scattered field[66].

2.3 Theory

We begin by describing the precise expression of multipole expansion as described in [74]. Let's start by defining the following situation: a plane wave with the amplitude of an

electric field $|\boldsymbol{E}_{\text{inc}}| = E_0$ at a frequency $\boldsymbol{f}$ illuminates an item in free space.$r = (x, y, z)$ is a definition of a position vector in a Cartesian coordinate system. $\boldsymbol{J}(\boldsymbol{r})$ can be calculated from the $\boldsymbol{E}(\boldsymbol{r})$ when incoming light excites the object by

$$\boldsymbol{J}(\boldsymbol{r}) = -i\omega\varepsilon_0(n^2 - 1)\boldsymbol{E}(\boldsymbol{r}) \tag{29}$$

In the given equation, ω represents the angular frequency, ε_0 represents permittivity (free space), and n represents the refractive indices of the resonator. It is important to mention that $\boldsymbol{J}(\boldsymbol{r})$ pertains to the distributions of displacement current in the dielectric Mie resonators. The multipole moments, specifically the magnetic dipole ($\boldsymbol{m}$), electric dipole ($\boldsymbol{p}$), magnetic quadrupole $\left(\hat{Q}^m\right)$, and electric quadrupole $\left(\hat{Q}^e\right)$, can be obtained through derivation.

$$p_\alpha = -\frac{1}{i\omega}\left[\int J_\alpha j_0(kr)\mathrm{d}^3r + \frac{k^2}{2}\int\{3(\boldsymbol{r}\cdot J)r_\alpha - r^2J_\alpha\}\frac{j_2(kr)}{(kr)^2}\mathrm{d}^3\boldsymbol{r}\right] \tag{29}$$

$$\begin{aligned}\hat{Q}^{\mathrm{e}}_{\alpha\beta} = -\frac{3}{i\omega}\Big[&\int\{3\left(r_\beta J_\alpha + r_\alpha J_\beta\right) - 2(\boldsymbol{r}\cdot J)\delta_{\alpha\beta}\}\frac{j_1(kr)}{kr}\mathrm{d}^3\boldsymbol{r}\\ &+ 2k^2\int\{5r_\alpha r_\beta(\boldsymbol{r}\cdot\boldsymbol{J})\\ &- r^2\left(r_\alpha J_\beta + r_\beta J_\alpha\right) - r^2(\boldsymbol{r}\cdot J)\delta_{\alpha\beta}\}\frac{j_3(kr)}{(kr)^3}\mathrm{d}^3r\Big]\end{aligned} \tag{30}$$

$$\hat{Q}^{\mathrm{m}}_{\alpha\beta} = 15\int\{r_\alpha(\boldsymbol{r}\times J)_\beta + r_\beta(\boldsymbol{r}\times J)_\alpha\}\frac{j_2(kr)}{(kr)^2}\mathrm{d}^3\boldsymbol{r}, \tag{31}$$

$$m_\alpha = \frac{3}{2}\int(\boldsymbol{r}\times J)_\alpha\frac{j_1(kr)}{kr}\mathrm{d}^3\boldsymbol{r} \tag{32}$$

The variables α and β are represented by x, y, and z, respectively. The variable k denotes the wavenumber. Please note that $jn(\rho)$ represents the spherical Bessel function, which is defined as

$$j_n(\rho) = \sqrt{\pi/2\rho} J_{n+1/2}(\rho) \tag{33}$$

Where $Jn(\rho)$ is the Bessel function of the first kind, by utilizing the derived multipole moments mentioned above, we can proceed to compute the total scattering cross section as described [62].

$$C_{\text{sca}}^{\text{total}} = \frac{k^4}{6\pi\varepsilon_0^2|E_0|}\left[\sum\left(|p|^2 + \left|\frac{m}{c}\right|^2\right) + \frac{1}{120}\sum\left(\left|\hat{Q}^{\text{e}}\right|^2 + \left|\frac{k\hat{Q}^{\text{m}}}{c}\right|^2\right) + \cdots\right] \tag{34}$$

Total scattering cross section can be expressed as the summation of partial scattering cross sections originating from various multipoles, denoted as $C_{\text{sca}}^{p}, C_{sca}^{m}, C_{\text{sca}}^{\hat{Q}^e}, and\ C_{\text{sca}}^{\hat{Q}^m}$

Subsequently, we demonstrate the mathematical expression while employing the long-wavelength approximation. The derivation of the approximated expression involves approximating the spherical Bessel functions [75]. The expression of the multipole moments is given by:

$$p_\alpha \approx -\frac{1}{i\omega}\left[\int J_\alpha \mathrm{d}^3 r + \frac{k^2}{10}\int\{(\boldsymbol{r}\cdot J)r_\alpha - 2r^2 J_\alpha\}\mathrm{d}^3 r\right] \tag{35}$$

$$m_\alpha \approx \frac{1}{2}\int(\boldsymbol{r}\times J)_\alpha \mathrm{d}^3 r \tag{36}$$

$$\hat{Q}^{\mathrm{e}}_{\alpha\beta} \approx -\frac{1}{i\omega}\Big[\int\{3(r_\beta J_\alpha + r_\alpha J_\beta) - 2(\boldsymbol{r}\cdot J)\delta_{\alpha\beta}\}\mathrm{d}^3 r + \frac{k^2}{14}\int\{4r_\alpha r_\beta(\boldsymbol{r}\cdot\boldsymbol{J}) - 5r^2(r_\alpha J_\beta + r_\beta J_\alpha) + 2r^2(\boldsymbol{r}\cdot J)\delta_{\alpha\beta}\}\mathrm{d}^3 r\Big] \tag{37}$$

$$\hat{Q}^{\mathrm{m}}_{\alpha\beta} \approx \int\{r_\alpha(\boldsymbol{r}\times J)_\beta + r_\beta(\boldsymbol{r}\times J)_\alpha\}\mathrm{d}^3 r. \tag{38}$$

Total scattering cross sections can be derived using the same mathematical expression as Eq. (34).

The multiple family is completed by the addition of toroidal moments. Since the electric dipole moment's higher-order term can be interpreted as toroidal dipole moment ($\boldsymbol{T}$), Mathematically, it can be expressed as follows.

$$p_\alpha \approx -\frac{1}{i\omega}\int J_\alpha \mathrm{d}^3 r \tag{39}$$

$$T_\alpha \approx \frac{1}{10c}\int\{(\boldsymbol{r}\cdot\boldsymbol{J})r_\alpha - 2r^2 J_\alpha\}\mathrm{d}^3 r. \tag{40}$$

The overall scattering cross section that corresponds is:

$$C^{\mathrm{total}}_{\mathrm{sca}} = \frac{k^4}{6\pi\varepsilon_0^2|E_0|}\Big[\sum\left(|p + ik\boldsymbol{T}|^2 + \left|\frac{m}{c}\right|^2\right) + \frac{1}{120}\sum\left(\left|\hat{Q}^{\mathrm{e}}\right|^2 + \left|\frac{k\hat{Q}^{m}}{c}\right|^2\right) + \cdots\Big]. \tag{41}$$

Please note that we have only introduced the concept of a toroidal dipole in this discussion. It is important to mention that a higher-order toroidal moment is also encompassed within the electric quadrupole moment. Additionally, it is feasible to consider the higher-order terms of the electric quadrupole moment, treating it as a

toroidal quadrupole moment. The anapole condition can be deduced from Equation (41) as $\boldsymbol{p}+ik\boldsymbol{T}=0$.

2.3.1 Anapole

Subwavelength photonic structures support the interference of electromagnetic modes, which is a fundamental concept that forms the basis for precisely manipulating light at the nanoscale in meta-optics. Numerous applications in low-loss nanoscale optical antennas, meta-surfaces, and meta-devices propel the field of all-dielectric Mie-resonant nano-photonics. The interaction between the electric and toroidal dipole moments gives rise to a distinct optical state known as the optical anapole, which exhibits low radiation characteristics.

Over the past decade, there has been a noticeable increase in the research focus on investigating different optical phenomena related to toroidal electrodynamics and Anapoles (see figure 7[69]). This interest is particularly evident in the fields of metamaterials and nano-photonics. The interest in this topic develops primarily from the numerous opportunities presented by the multipolar response of subwavelength optical structures. These structures enable a more comprehensive understanding of various optical phenomena at the nanoscale, such as multipolar nonlinear nano-photonics[76].

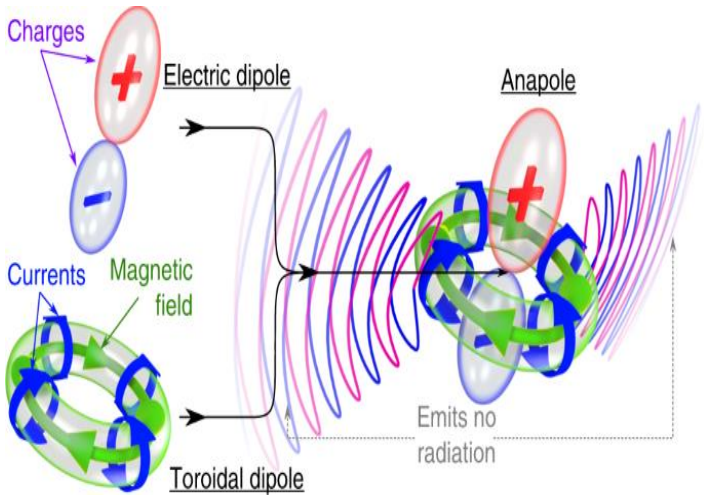

Figure 7 Structure of a dynamic anapole[77].

The growing interest in toroidal multipoles can be attributed to the increasing recognition that, in addition to electric and magnetic multipoles, it plays a vital role in fully characterizing the electromagnetic properties of matter [78]. The characterization of electromagnetic fields in free space involves the use of and transverse magnetic (TM) and transverse electric (TE) multipoles[62]. However, three different multipole series are required when characterising the current density: electric, magnetic, and toroidal multipoles see figure 8 [79].

The unique function of toroidal multipoles becomes evident in the optical characteristics of materials that consist of sizable molecules or structural components with toroidal symmetry comparable on a scale comparable to the electromagnetic wavelength. The investigation of the dynamic toroidal response in metamaterials has been a topic of significant discourse since 2007 [79]. However, the initial unequivocal experimental validation of the prevailing toroidal response in matter was documented in a microwave metamaterial in 2010 [80]. Following that, the phenomenon of dynamic toroidal response has been published in various types of materials, including metallic [81], plasmonic[82], and dielectric metamaterials[83]. These observations have been made

across a wide range of frequencies, spanning from micro to terahertz and extending to the near-infrared and visible regions of the electromagnetic spectrum. A comprehensive understanding of transmission, reflection [81], and polarization phenomena[84] in metamaterials and complex molecular systems necessitates including dynamic toroidal response. Toroidal resonances have the potential to contribute significantly to the functionality of nano-lasers [85], sensors [86], and data storage devices [87]. It is also worth mentioning that static toroidal dipoles are referred to as "static anapole", as introduced by Ya. B. Zeldovich, in nuclear physics[81], has been observed in magnetism [88]. These dipoles could be the sole permissible electromagnetic form factor for dark matter candidate particles [89].

The combination of an electric dipole, consisting of pairs of oscillating charges, and a toroidal dipole, which has an oscillating poloidal current on a torus see figure 8, can give rise to a charge-current configuration known as a "dynamic anapole"[90]. The absence of radiation characterizes this configuration. The anapole state is observed at a specific frequency of oscillations, where the fields emitted by the electric and toroidal dipoles, which are located nearby, cancel out each other through the phenomenon of destructive interference. It is important to note that electric and toroidal dipoles exhibit identical radiation patterns, as shown in Figure 8. Consequently, the overall emission of an anapole is zero. Anapoles that are perfectly formed do not indicate any emission or absorption of light, making them undetectable through far-field observations. The detection of anapole excitations is contingent upon their (weak) coupling to electromagnetic modes that interact with free-space radiation. Alternatively, detection is possible if the anapole excitations are not perfectly balanced, meaning that the electric dipole emission does not completely cancel out the toroidal dipole radiation. A slightly off-balanced anapole configuration will result in a narrow scattering spectrum peak. The initial observation of electromagnetic anapoles occurred when narrow transmission peaks were detected in the spectra of a microwave metamaterial in 2013 [91]. Anapole

excitations have been observed in dielectric nanoparticles[92] as well as in metallic[93] and plasmonic metamaterials[94].

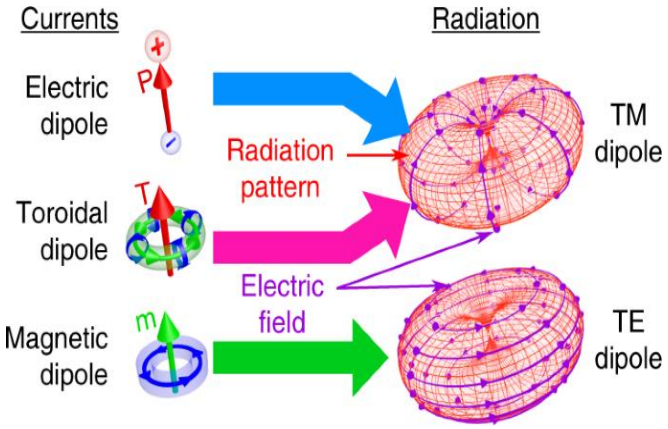

Figure 8 Radiation patterns of the electric (p), magnetic (m) and toroidal (T) dipoles[77].

2.3.2 Kerker Effect

In 1983, an intriguing phenomenon was observed by Milton Kerker and his colleagues [95] during their study on the scattering of electromagnetic waves by a spherical particle composed of a magnetic material. This material exhibited specific properties such as dielectric permittivity ϵ , and magnetic permeability (μ). The present work has uncovered a highly distinctive phenomenon, commonly referred to as the Kerker effect, in contemporary scientific discourse. Kerker and his group demonstrated the potential to manipulate the direction of scattered radiation based on the frequency, whether in forward or backwards. Two Kerker conditions were found. The first Kerker condition is associated with eliminating backward scattering, resulting in a peak in forward scattering.

Conversely, the second Kerker condition is characterised by a significant decrease in light scattering in the forward direction, leading to a deep minimum. The concepts of backward and forward scattering refer to the scattering along the incoming axis waves.

The optical theorem is a principle that relates the extinction cross-section of a scatterer to its forward scattering. It implies that the forward scattering cannot be cancelled or eliminated. Kerker et al. determined that the first condition is met when ϵ = μ, and the second condition is fulfilled when.

$$\epsilon = -\frac{\mu - 4}{\mu + 1} \tag{42}$$

The initial dissemination of this significant study was limited due to the unavailability of necessary magnetic materials and the specific parameter values required by the Kerker conditions.

The Kerker conditions are determined by calculating the magnetic and electric polarizabilities of the dielectric scatterer, denoted as α_e and α_h, respectively. The electric and magnetic polarizabilities can be conveniently obtained by analysing the element of the $T_n^{(e,h)}$ matrix, where *h* and *e* represent magnetic and electric properties, respectively. These elements are conventionally denoted as a_n and b_n, with *n* representing the multipolar orders.

$$\alpha_e = -T_n^{(e)} = \frac{3\mathrm{i}\epsilon a_1}{2k^3} \tag{43}$$

$$\alpha_h = -T_n^{(h)} \frac{3\mathrm{i}b_1}{2\mu k^3} \tag{44}$$

In the case of a dipolar scatterer, which refers to a scatterer where the multipolar Mie scattering coefficients a and bn can be ignored for *n ≥ 2*, the first Kerker condition is met when a_n is equal to b_n. Similarly, the second Kerker condition is satisfied when the following relationships hold: the real part of $(\epsilon^{-1}\alpha_e)$ is equal to the negative real part of $(\mu\alpha_m)$, and the imaginary part of $(\epsilon^{-1}\alpha_e)$ is equal to the imaginary part of $(\mu\alpha_m)$[96].

2.3.3 Fano Resonance

The phenomenon of Fano resonance is widely observed in various domains where wave propagation and interference can occur. The phenomenon of Fano resonance arises from the interference between broad and narrow radiation spectra. It has emerged as a significant tool in various applications in physical, chemical, and biological sciences.

Resonances are all around us in the world. The human environment encompasses a wide array of natural and artificial resonators, ranging from musical instruments to intricate technological devices such as lasers and medical-imaging machines. Resonances serve as a fundamental principle in the field of photonics. The Fano resonance occurs when a discrete quantum state interferes with a continuous band of states, leading to manifestation in the absorption spectrum (E). The legendary Fano formula delineates the distinctive shape:

$$\sigma(E) = D^2 \frac{(q + \Omega)^2}{1 + \Omega^2} \tag{45}$$

In this context, the symbol E represents the energy, $q = \cot\delta$ is denoted as the Fano parameter, and δ signifies the phase shift of the continuum. Additionally, Ω is defined as $2(E - E_0)/\Gamma$, where Γ represents the resonance width and E_0 corresponds to the energy. Lastly, D^2 is expressed as $= 4\sin^2\delta$ [97]. Eq (45) demonstrates broad applicability, encompassing absorption and various optical spectra, such as transmission and scattering, across diverse systems. Recently, there has been a significant surge in interest surrounding Fano resonance, primarily driven by advancements in the field of photonics, which pertains to the study of objects exhibiting multiple resonant properties. Undoubtedly, nearly every resonant state possesses characteristics that allow it to be regarded as quasi-discrete, exhibiting a complex frequency that can be effectively characterised through the concept of Fano resonance. The study of Fano resonances in photonics has garnered significant attention due to the pronounced transmission-

reflection curves that arise from this phenomenon, characterised by a distinct transition from complete transmission to reflection. This feature serves as a compelling foundation for various switching devices within the field of photonics[98].

3 Experimental Work

3.1 3D Printing (Phrozen Sonic Mini 8K)

Three-dimensional (3D) printing is a significant field within Research and Development (R&D) departments. It is attributed to the efficient rapid prototyping process, which allows for swift identification and elimination of design errors and facilitates product improvements during the prototyping stage. This approach effectively expedites the implementation of new solutions while minimizing production costs and eliminating the need for in-production testing of incomplete models. Using 3D printing techniques has facilitated the efficient creation of prototypes featuring intricate geometries within a significantly reduced timeframe while maintaining unparalleled precision[56].

3.1.1 Liquid Crystal Display 3D Printing

The advent of additive manufacturing (AM) technology has revolutionized various industries, such as machinery, aerospace, and electronics. One of the primary concerns in today's industry is the implementation of efficient, accurate, and practical procedures in additive manufacturing (AM). Liquid crystal display (LCD) is one of the additive manufacturing technologies.

An LCD screen was utilized in the process of 3D printing. A liquid crystal display (LCD) matrix was positioned along the optical pathway connecting the lamp and the vat containing the photosensitive material. The system, equipped with an appropriate beam-forming lens, generates an object profile within the resin. The LCD-DLP (Digital Light Processing) system is typically distinguished by its higher resolution compared to the DMD (Digital Micromirror Device) system [99]. In the context of LCD matrices, the energy supplied to the photosetting resin is constrained due to the significant absorbance

exhibited by the LCD matrix. The absorbance of the matrix material shows wavelength-dependent variations, effectively filtering radiation below 400 nm[100].

That is why LED bulbs with a wavelength of 405 nm or higher are used in most new printer designs. Even with powerful lights, visible light is still rather low. As a result, materials that need a high light intensity for photopolymerization are hampered. Figure 9 depicts a 3D printer that uses an LCD-DLP light source[101].

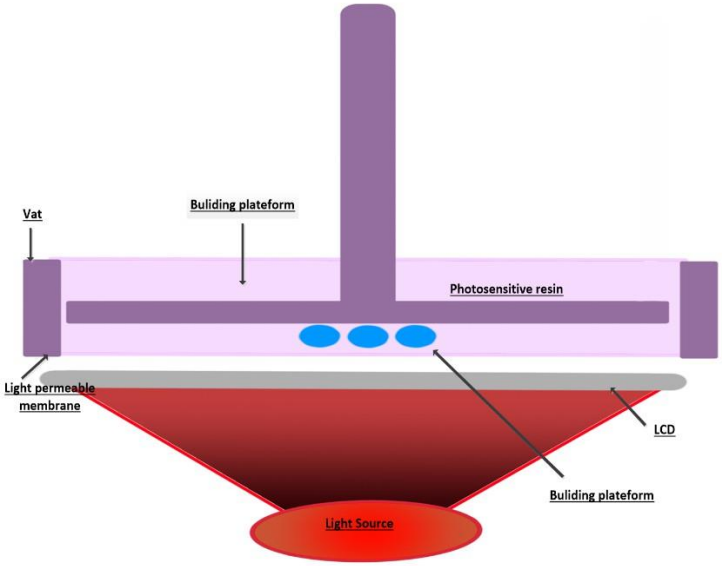

Figure 9 A schematic depiction of an LCD–digital light processing (DLP) 3D printer.

3.1.2 (Phrozen Sonic Mini 8K)

The Sonic Mini 8K boasts an LCD module with a resolution of 7500 X 3240 pixels, surpassing any competing product currently available. This exceptional pixel count enables the creation of truly remarkable and highly detailed models. The Sonic Mini 8K offers outstanding output quality and a prebuilt design that ensures convenience. Its straightforward calibration enhances the overall user experience, delivering a seamless out-of-the-box setup.

1.	Machine Footprint	(11.4 × 11.4 × 16.5) inch
2.	Build Volume	(6.5 × 2.8 × 7) inch
3.	UV light	Linear Projection LED Module
4.	Resin	DLP Photopolymer Resin
5.	Masking LCD Resolution	7500 × 3240
6.	Masking LCD Size	7.1 inch
7.	Touch Screen	3.5 inch

Table 1 Specification of Phrozen Sonic Mini 8K

3.1.3 Printing Safety

Like other resin printers, the Phrozen Sonic Mini 8K must be used carefully. The chemicals used to clean your prints might irritate your skin, and uncured resin is harmful. When handling uncured prints and pouring resin, wear gloves and safety eyewear.

3.1.4 Slicer Compatible & Printing flow work

ChituBox and Lychee Slicer's newest releases are supported by the Phrozen Sonic Mini 8K. Slicing software for resin 3D printers enables you to conserve resin by adding supports, hollowing your product, and adding drain holes. Since printer settings might vary depending on resin brand, kind, and ambient temperature, you should do exposure testing before beginning printing. An exposure test is a part of Phrozen.STL data. CTB

files can be put onto a USB drive and inserted into the machine's front slot once sliced. Click the Print button, pick your file, and press the Go button, as seen in figure 10.

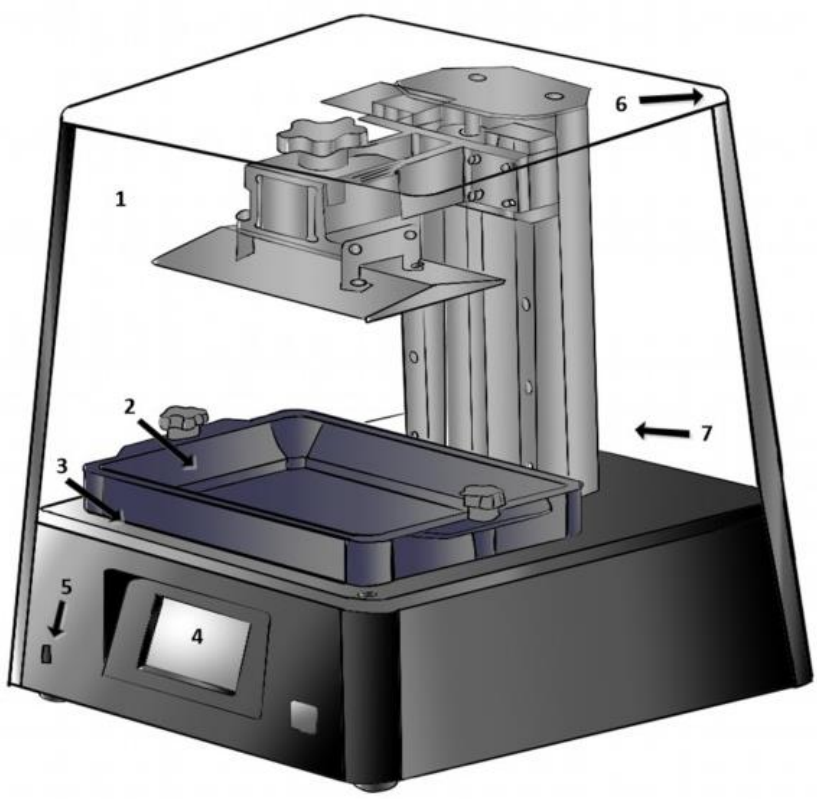

Figure 10 (1). Building plate (2). Resin Vat (3). LCD screen (4). Touch Panel (5). USB Port (6). Plastic Case (7). Z- axis

3.1.5 Washing and Curing

You must wash and cure your prints before you can view them. It is recommended to perform a 30-second wash using 95% Isopropyl alcohol, followed by a subsequent immersion in a separate container containing cleaner IPA. A soft brush is recommended for effectively cleaning hard-to-reach areas and crevices.

Please ensure that the print is thoroughly dried using a dryer set to a cool temperature. Any residual IPA (isopropyl alcohol) on the print may cause it to appear white.

Additionally, allowing the printed material to dry naturally in a location not exposed to direct sunlight is advisable.

Since 3D structures are so much softer, they must be removed before the print is UV cured. Remove the 3D design with side cutters and tweezers. Wearing gloves is mandatory while working with uncured prints.

After that, leave the printed structure in direct sunshine for a few hours or in a UV curing station for a few minutes.

Never dump your IPA down a sink, especially if it has been tainted with uncured resin. Use the resin until it becomes too filthy, then leave the container open so that it can evaporate. The sun or UV radiation might cure the residual sludge before disposal.

3.2 Sample Fabrication

A graphene-like film (NiPPF) was produced on a silica substrate using a nickel catalyst-assisted pyrolysis process at an elevated temperature. The silica substrate was coated with a 10 nm-thick nickel catalyst layer. The catalyst layer was deposited onto the substrate using Sputter Quorum Q300TT Plus. Subsequently, the sample underwent spin-coating with a resist layer measuring 230 nm thick. The resist film applied using the spin-coating technique underwent a prebaking process for 1 minute at a temperature of 110 °C.

The substrate, consisting of a sacrificial Ni nanolayer and spin-coated resist film, was annealed in a chemical vapor deposition (CVD) chamber. The annealing process took place at a temperature of 800 °C within a hydrogen (H2) atmosphere with a flow rate of 5 standard cubic centimeters per minute (sccm) and a pressure of 1 millibar (mbar)[102]. The annealing duration lasted for a total of 10 minutes. Through conducting pyrolysis at various thicknesses of the Ni layer, it has been determined that, given our specific experimental conditions, the most favourable thickness for the Ni layer is 10 nm. The

synthesized NiPPF exhibits similarities to multilayered graphene in terms of crystallinity, thickness, and surface conductivity at this specific thickness. Additionally, it demonstrates mechanical durability and strong adhesion to the dielectric support material[103].

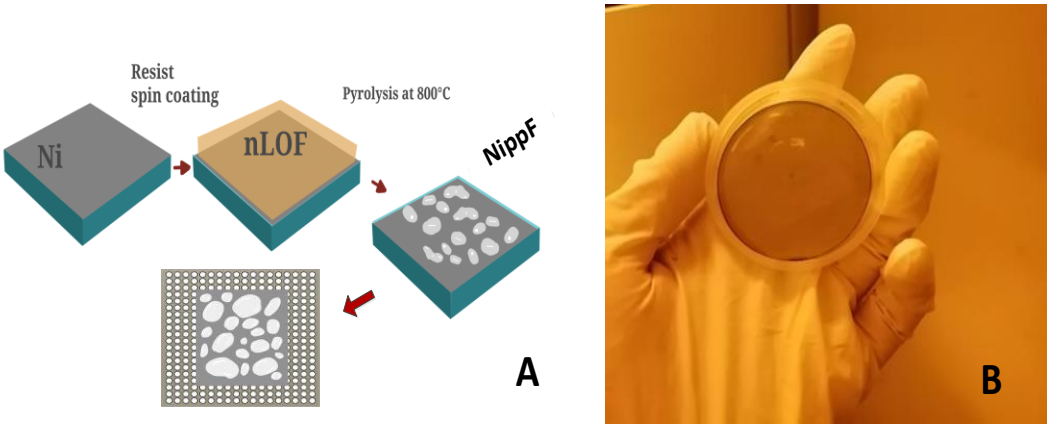

Figure 11 illustrates the process flow to synthesize NiPPF on a dielectric substrate (B), Resulting NiPPF.

The pyrolysis of the photoresist film occurs at temperatures exceeding 600 °C, while the Ni-assisted conversion of PPF into NiPPF is initiated within the temperature range of 700-800 °C[104]. The solvent in the resistive layer evaporated upon achieving a temperature of 700 °C. Under identical temperature conditions, the nickel film undergoes a retraction process, forming nickel islands with submicron dimensions[103].

3.3 Terahertz Spectroscopy

Terahertz spectroscopy is a powerful time-domain spectroscopy (THz-TDS) technique that focuses on the production and coherent detection of terahertz radiation. This form of radiation falls between microwaves (MW) and infrared (IR) waves within the electromagnetic spectrum, as depicted in figure 12. It serves as a valuable analytical tool for characterising specimens of interest. Terahertz (THz) pulses play a crucial role in the electromagnetic (EM) flow, ranging from a few picoseconds. These pulses consist of frequencies ranging from approximately 0.1 to 10 THz, corresponding to a photon energy

of around 4.1 meV. They exhibit an electromagnetic field with alternating periods of approximately 3 ps to 10 fs. Due to their unique characteristics, THz pulses seek extensive applications in various scientific and engineering disciplines[105].

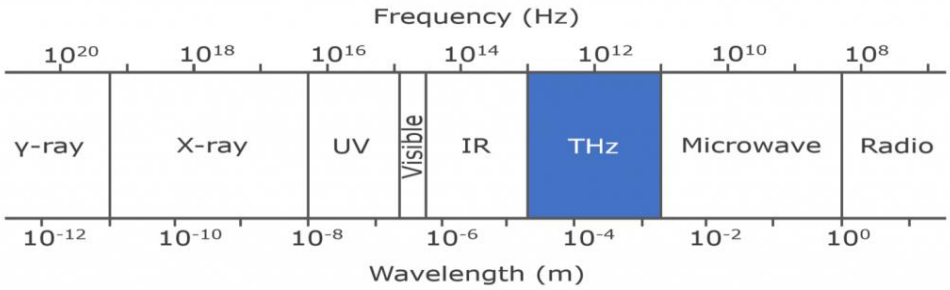

Figure 12 Schematic of EM spectrum showing the position of THz band O.1 -10 THz.

The terahertz (THz) radiation commonly employed in terahertz time-domain spectroscopy (THz-TDS) typically exhibits broadband characteristics. It is achieved by utilising a femtosecond laser with ultrashort pulses and applying a bias to a photoconductive antenna at approximately 800 nm and 100 fs. The pulses emitted by the femtosecond laser are initially divided by a 50:50 beam splitter (BS), with a portion being transmitted and another being reflected, as depicted in figure 13.

The transmitted pulses are directed towards two micromirrors, M1 and M2, which are positioned at a 45-degree angle to each other within a delay stage. The reflected pulses are then focused onto a separate mirror, M3. The pulses are subsequently reflected from mirror M3 onto mirrors M4 and M5, which are positioned on a motorised delay stage. The pulses from M5 are reflected at a normal incidence on parabolic mirrors (P1, P2, and P3). These mirrors, in turn, reflect the pulses onto the THz source/emitter, effectively serving as the input THz source. The pulses are subsequently collimated or focused onto the surface of the sample.

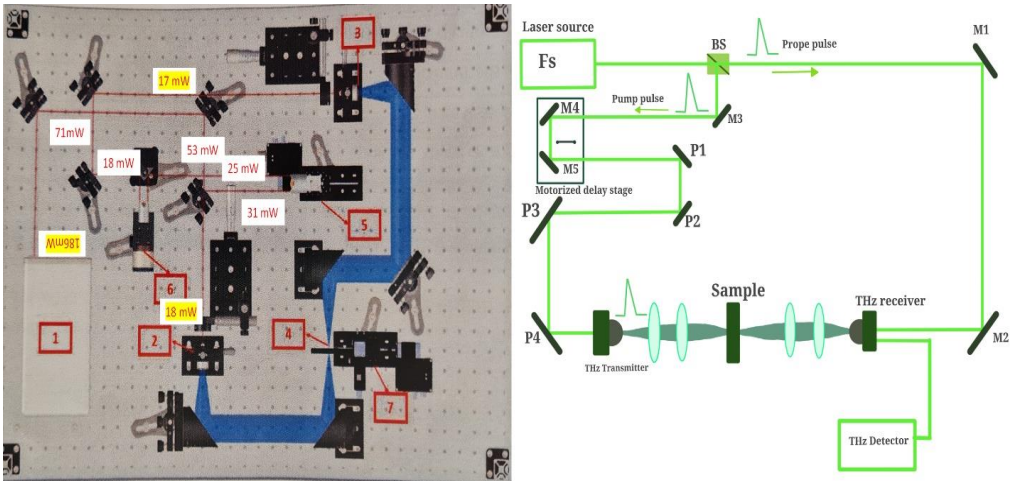

Figure 13 Schematic representation of the THz time-domain spectroscopy

The output pulses propagating through the sample's surface are subsequently directed towards a THz receiver. This receiver effectively combines with the transmitted pulses and focuses them onto the THz detector for detection[106]. The time-domain pulses can be converted into frequency-domain pulses using the Fourier transform and the appropriate modulation depth derived from the obtained results. Through THz time-domain spectroscopy, comprehensive investigations can be conducted to analyse the modulation depth of a sample, whether it is achieved through reflectance or transmittance from the active device.

4 Result and Discussion

4.1 Modelling result

Due to the diverse characteristics of graphene-like film (NiPPF) and its distinct electromagnetic properties, the simulation of its behaviour presented a significant and formidable challenge. Our main goal was to investigate the electromagnetic field characteristics of a voids structure periodically arranged with precise dimensions: a diameter of 310 micrometres and a height of 50 micrometers, as shown in figure 14D.

Based on the reliable simulation results, the subsequent logical progression was to actualize the design. Utilizing advanced 3D printing technology, we carefully manufactured the voids structure, ensuring the precise replication of its dimensions and properties per the simulated model.

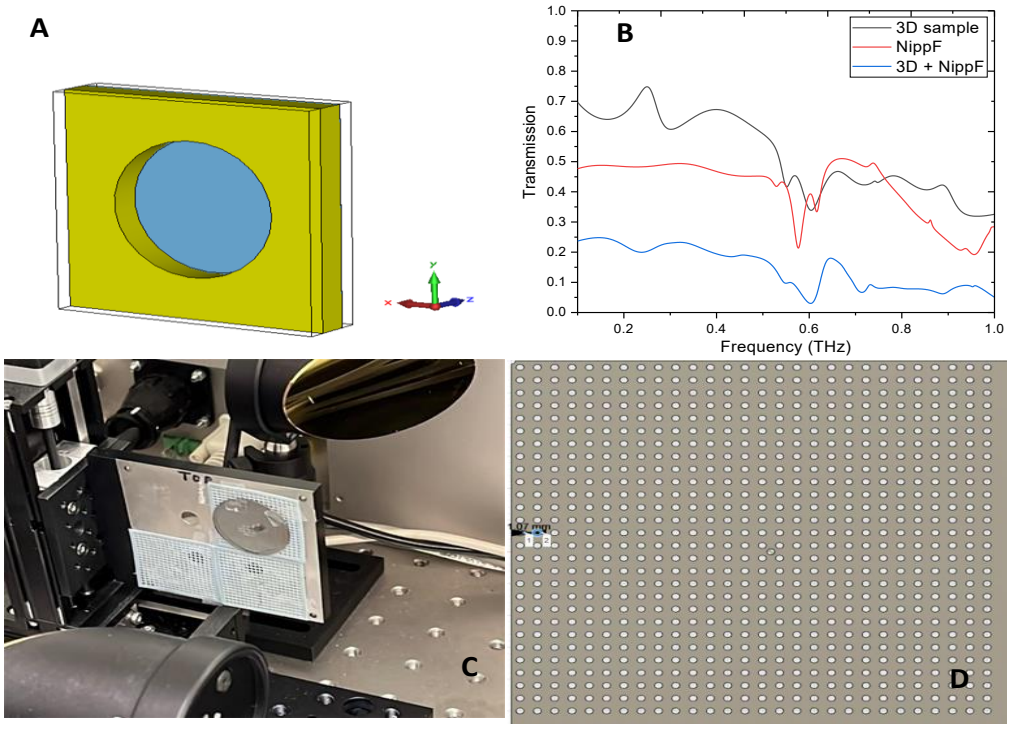

Figure 14 (A) Simulation Image (void) (B) Resulting plots of Voids (C) 3D printing coupled with NiPPF (D) Periodically arranged voids.

The final stage of this project involved the characterization phase, during which the high absorption properties of the 3D printed structure were evaluated in real-world conditions. This phase played a crucial role in validating the simulation results. It offered valuable insights into the potential applications of the graphene-like film (NiPPF) and voids structure in photonics.

The optical and electromagnetic characteristics of metamaterials are highly dependent on their size. Table 2 shows a discernible growth pattern in the samples' diameters and heights. This systematic scaling up makes it possible to investigate the effects of size variation on the photonic characteristics of the materials in detail.

Thus, our experiments and simulations show that 3D materials combined with thin conductive films like NiPPF can be promising as ideal absorbers for THz application. Nevertheless, NiPPF's conductivity, especially 3D dielectrics, is very low compared to metals; the transmission through the system is suppressed due to the resonance nature of multiple scattering between layers. Thus, we can expect that 3D printing materials with graphene-like films can be applied as elements of THz photonics and biophotonics due to eco-friendly materials.

Sample names	**Diameter μm**	**Height μm**
Case 1	310	50
Case 2	620	100
Case 3	930	150
Case 4	630	100
Case 5	930	150
Case 6	1240	200

Table 2 Different sample cases and their parameters

Case 1

Based on the results of our simulations, we have decided to materialize our digital model by utilising 3D printing technology. We used Autodesk Fusion 360 software to design a void structure with precise dimensions. The voids exhibit a diameter of 310 micrometers and a height of 50 micrometers, aligning precisely with the anticipated outcomes of our simulations.

Nevertheless, we encountered an obstacle during the printing procedure. The initial design did not incorporate a substrate; however, during the 3D printing process, a thin layer measuring 0.5 micrometers was introduced beneath the voids. The inclusion of this unexpected element has prompted us to consider its potential impact on our findings.

To enhance our comprehension, we produced two iterations of the voids: one utilizing a thin substrate and another aimed at closely replicating our original design (without substrate), as shown in figure 15.

After completing the 3D printing process for our structure, we proceeded with an essential post-processing step. To explore the potential advantages of UV curing, we subjected the sample to 24 hours of UV light exposure. This treatment aimed to improve the stiffness and alignment of our printed structure, ensuring it adhered to the specified requirements and demonstrated optimal performance attributes.

After completing the UV curing process, we assessed the transmission properties of our sample through terahertz (THz) measurements. The utilization of Terahertz spectroscopy, due to its capability to effectively penetrate diverse materials and offer comprehensive insights into their internal structures, was deemed an optimal selection for our analysis.

The results of our study are consolidated in Table 3, which displays the average transmission and absorption rates for the two samples. The data provides valuable

insights into the UV curing process's impact on the sample's transmission properties. It highlights the significance of post-printing treatments to achieve desired outcomes.

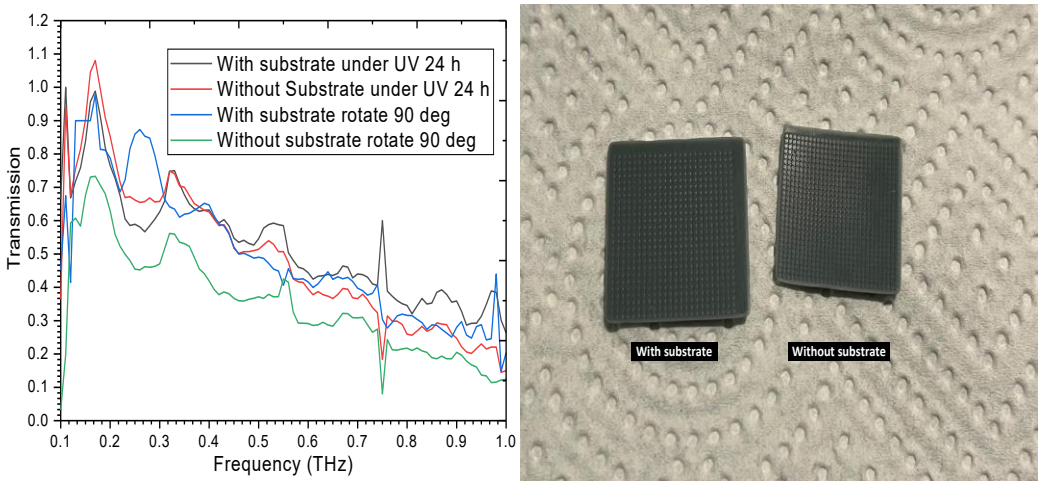

Figure 15 Left side THz transmission of a 3D sample, right side 3D printed samples

Plot Names	Average (T)	Average (A)
With Substrate under UV 24 h	0.534	0.466
Without Substrate under UV 24 h	0.557	0.443
With Substrate rotate 90	0.525	0.475
Without Substrate under rotate 90	0.386	0.614

Table 3 Average Transmission (T) and Absorption (A) of case 1 (diameter 310 and height 50) μm

Case 2

We conducted multiple iterations of printing various structures to establish congruence between our experimental findings and the simulations. Notwithstanding these endeavours, the desired results remained difficult to achieve.

We modified the structure's dimensions during a single iteration, producing voids with a diameter of 620 micrometers, a height of 100 micrometers, and a spacing between the voids. After printing, we carried out the same post-processing steps as we did with our previous sample from 'Case 1'. This involved subjecting the printed material to a 24-hour UV curing process.

After conducting additional THz measurements on the modified structure, we observed variations in the average transmission and absorption value higher than our previous results, as shown in Table 4. The findings underscore the difficulties of precisely replicating simulated designs using 3D printing technology. Furthermore, they underscore the imperative nature of ongoing refinement in the experimental methodology.

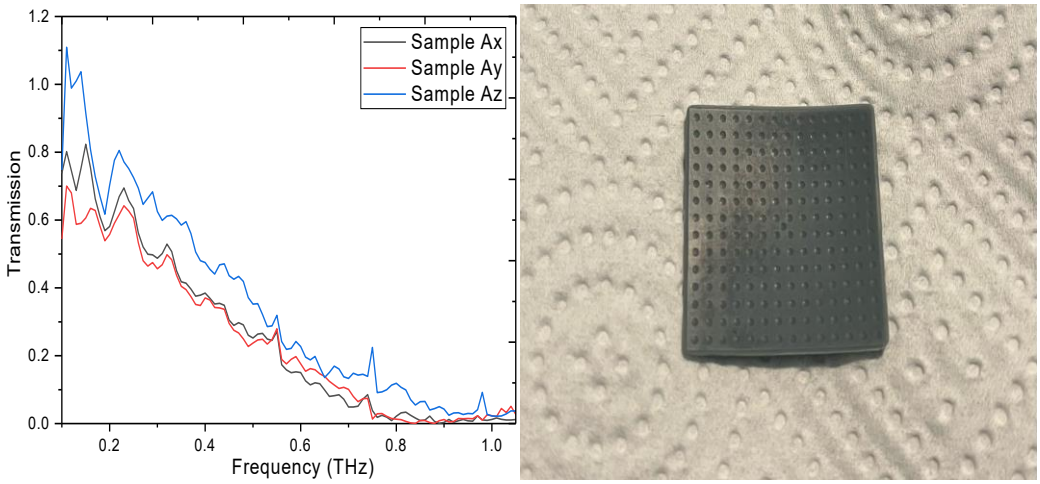

Figure 16 Left side THz transmission of a 3D sample, right side 3D printed sample.

Plot Names	Average (T)	Average (A)
Sample Ax	O.751	0.249
Sample Ay	0.632	0.368
Sample Az	0.428	0.572

Table 4 Average Transmission (T) and Absorption (A) of case 2 (diameter 620 and height 100) µm

Case 3

Based on the findings from 'case 2', we endeavoured to enhance our framework to correspond more effectively with our simulation projections. The dimensions have been modified to a diameter of 930 micrometers and a height of 150 micrometers, reducing the spacing between them.

After successfully completing the 3D printing process for the modified structure, we performed THz measurements to assess its transmission and absorption properties. The findings revealed a significant increase in absorption and a corresponding decrease in transmission. Based on this observation, it can be inferred that the modification in dimensions and spacing between them have impacted the interaction between the structure and terahertz waves, resulting in the observed alterations in its optical properties.

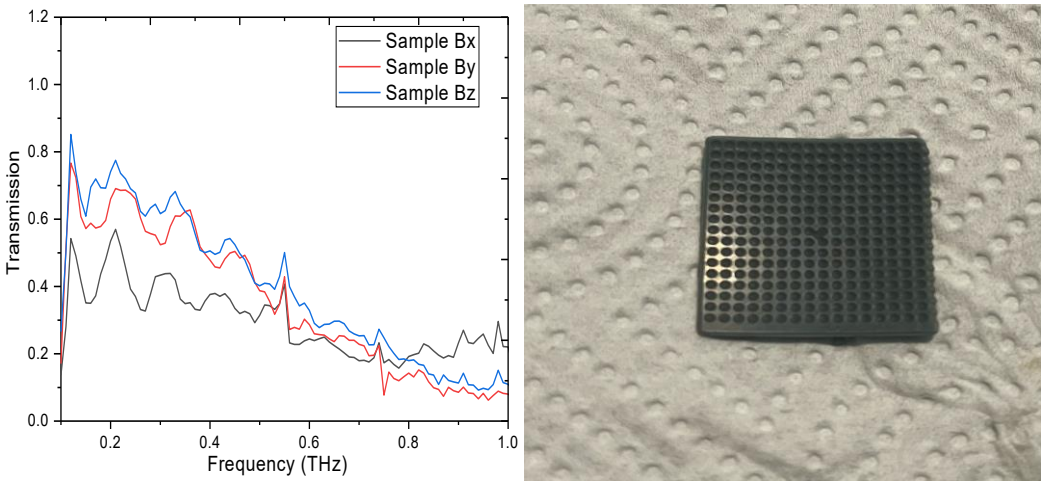

Figure 17 Left side THz transmission of a 3D sample, right side 3D printed sample

Plot Names	Average (T)	Average (A)
Sample Bx	0.339	0.661
Sample By	0.294	0.706
Sample Bz	0.412	0.588

Table 5 Average Transmission (T) and Absorption (A) of case 3 (diameter 920 and height 150) µm

Case 4

Based on the findings from 'case 3', we have taken the opportunity to revisit the design discussed in 'case 2' and adjusted by decreasing the spacing between the voids and keeping the diameter and height the same (620, 100 micrometers). The objective of this adjustment was to enhance the interaction between the structure and terahertz waves.

The findings obtained from the enhanced design demonstrated significant enhancements compared to 'case 2'. We have observed a decrease in transmission and an increase in absorption, suggesting a raised efficiency in the interaction between the structure and the THz waves.

To optimize the properties of the structure, we taped a Graphene-like film, referred to as 'NiPPF', onto the 3D sample, as shown in figure 18. It was hypothesized that the inclusion of this addition would impact the transmission and absorption characteristics of the structure, owing to the unique EM properties of NiPPF.

After conducting additional terahertz (THz) measurements following the application of NiPPF, we obtained even more promising results. According to the information presented in 'Table 6', the inclusion of the NiPPF resulted in notable modifications to the optical properties of the structure, demonstrating a closer alignment with our intended objectives.

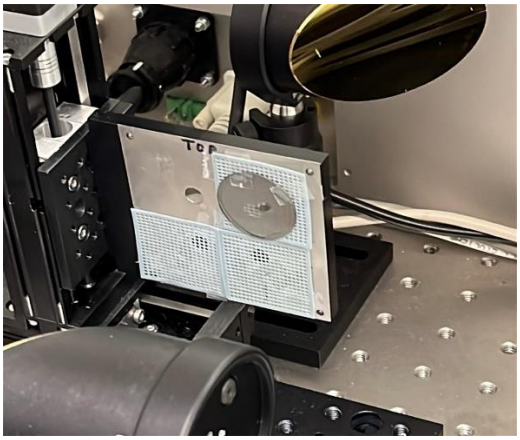

Figure 18 NiPPF on top of a 3D sample

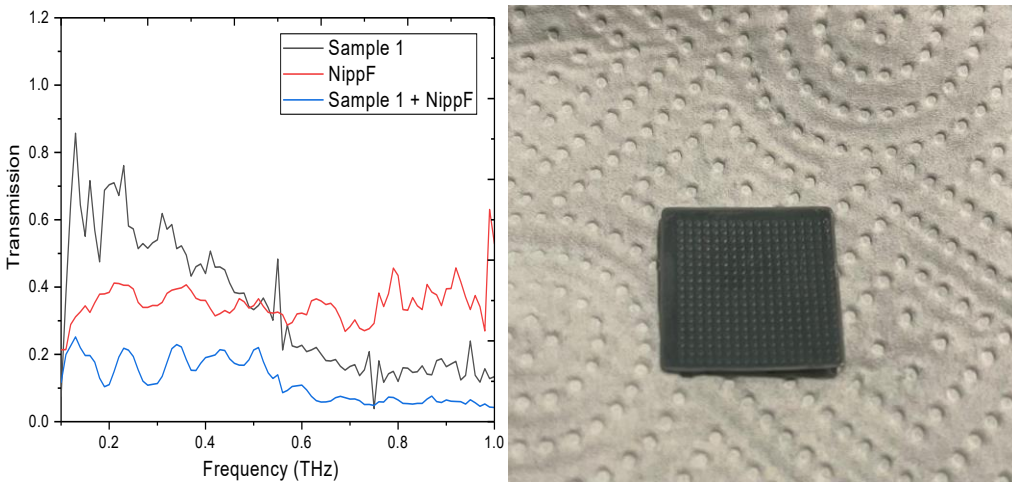

Figure 19 Left side THz transmission of a 3D sample, right side 3D printed sample

Plot Names	Average (T)	Average (A)
Sample 1	0.307	0.693
NiPPF	0.409	0.591
Sample 1 + NiPPF	0.211	0.789

Table 6 Average Transmission (T) and Absorption (A) of case 4 (diameter 620 and height 100) µm

Case 5

As part of our ongoing efforts to enhance the properties of the structure, we have proceeded to 'case 5', taking inspiration from the insights gained from 'case 4'. As per the specifications outlined in 'case 3', we have made a primary adjustment to the design by reducing the gap between the voids while ensuring that the dimensions, with a diameter of 930 micrometres and a height of 150 micrometres, remain the same. The rationale behind this modification was derived from the hypothesis that a more proximate configuration could potentially enhance the interaction between the structure and terahertz waves.

A NiPPF was applied to the 3D sample to optimise the structure's performance. This measure assessed the collective transmission and absorption characteristics of both the 3D structure and the Graphite film. The inclusion of graphene-like film, known for its unique electromagnetic characteristics, was anticipated to introduce further fluctuations in the optical properties.

The findings yielded positive outcomes. According to the information in 'Table 7', the combined structure demonstrated a notable reduction in transmission and increased absorption compared to 'case 4'. The results indicate that the improvements implemented in 'case 5', along with the incorporation of the Graphene-like film, enhanced the effectiveness of the interaction with THz waves, bringing us closer to our intended goals.

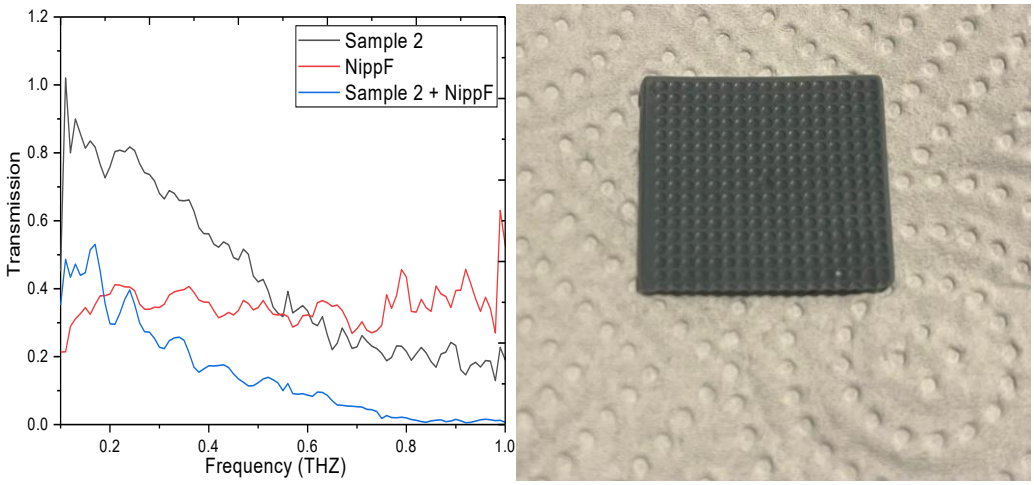

Figure 20 Left side THz transmission of a 3D sample, right side 3D printed sample.

Plot Names	Average (T)	Average (A)
Sample 2	0.597	0.403
NiPPF	0.409	0.591
Sample 2 + NiPPF	0.195	0.805

Table 7 Average Transmission (T) and Absorption (A) of case 5 (diameter 930 and height 150) µm

Case 6

Building upon the insights and findings from previous cases, particularly cases 4 and 5, we embarked on the next phase of our research journey: 'case 6'. A recurring challenge, as identified in our earlier experiments, was the inherent presence of a substrate during the 3D printing process. While necessary for the printing mechanism, this substrate introduced variables that could potentially influence our results.

Drawing from the positive outcomes of increasing dimensions in cases 4 and 5, we hypothesized that further enlarging the structure might bring us closer to our desired transmission and absorption properties. Consequently, the dimensions were adjusted to a diameter of 1240 micrometers and a height of 200 micrometers.

However, the structural transformation was the most significant departure in 'case 6'. We successfully printed our structure (voids without substrate), as shown in figure 21. This design was both innovative and strategic, aiming to optimise the structure's interaction with terahertz waves.

The results were compelling. As shown in the figure, the successfully printed 'voids' structure showcased a marked decrease in transmission and a corresponding increase in absorption. This outcome validated our design choices and underscored the importance of iterative experimentation and adaptation in achieving research objectives.

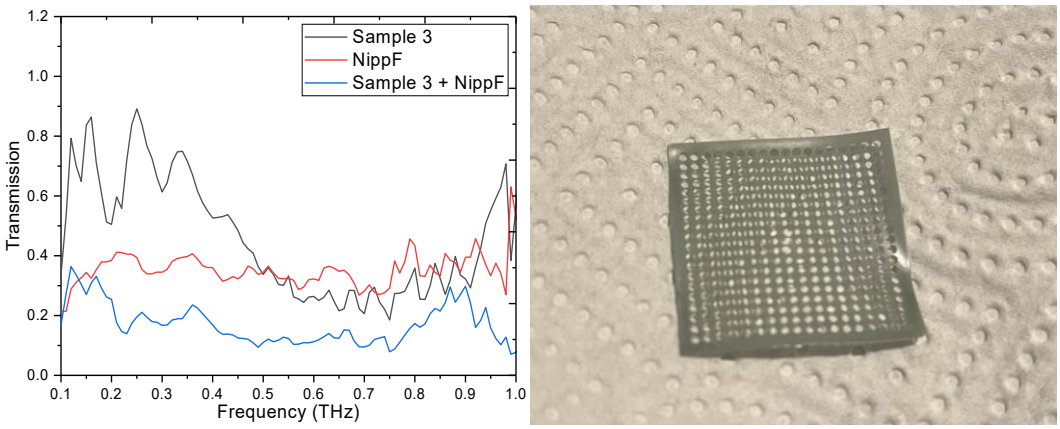

Figure 21 Left side THz transmission of a 3D sample, right side 3D printed sample.

Plot Names	Average (T)	Average (A)
Sample 3	0.673	0.327
NiPPF	0.409	0.591
Sample 3 + NiPPF	0.145	0.855

Table 8 Average Transmission (T) and Absorption (A) of case 6 (diameter 1240 and height 200) µm

5 Conclusion

This thesis examines the potential of graphene-like film metasurfaces for the absorption of terahertz (THz) radiations, especially utilising samples that were 3D printed. With its distinct characteristics, graphene-like film has been recognised as a potential ultra-thin absorber in the THz frequency band.

The main study samples are 3D-printed voids with the following specifications: 310 micrometres in diameter and 50 micrometres in height. UV curing was used throughout the 3D printing process to guarantee the uniformity and structural integrity of the voids. After printing, the samples were prepared for future analyses and testing using a standard sample preparation technique.

Throughout this project, numerical simulations and hands-on experimentation were employed to delve into the electromagnetic properties of voids structures. Utilizing COMSOL Multiphysics, we simulated the multipole expansion to understand the electromagnetic effects on a voids particle with specific dimensions: a diameter of 310 micrometres and a height of 50 micrometres.

One initial challenge was the inherent presence of a substrate during the 3D printing process. However, various structural designs were printed with varying dimensions, driven to achieve optimal transmission and absorption properties. The iterative process of adjusting diameters, heights, and spacing between the voids provided valuable insights. Notably, it was observed that structures with larger voids sizes and reduced spacing between them exhibited decreased transmission and increased absorption.

This research underscores the intricate balance between design dimensions and electromagnetic properties. The findings highlight the potential of tailored 3D printed

structures in achieving desired electromagnetic responses, paving the way for further innovations in THz technology.

The last result in our series was "case 6," where we saw significant absorption and low transmission. This result from the graphene-like film metasurface confirms the viability of our design modifications and the effectiveness of 3D printing in generating desired THz capabilities.

The electromagnetic response of the graphene-like film 3D printed array is examined in the THz frequency range. The primary objective is to validate the potential of the graphene-like film 3D printed structure as an ideal ultrathin absorber for THz radiations.

The operational principle employed centers around THz radiation and its detection. The samples are exposed to ultrashort laser pulses with a 1050 ± 40 nm wavelength. These pulses have a duration ranging from 5 to 150 fs and are emitted at a power level of 40 mW. This setup ensures a comprehensive interaction between the THz radiation and the graphene-like film structure, allowing for an in-depth analysis of its absorption capabilities.

The results gathered in the time domain are transformed into the frequency domain for data analysis. This conversion is facilitated using the Fast Fourier Transform (FFT) method, enabling a more detailed understanding of the electromagnetic response of the graphene-like film 3D printed array.

The experiments conducted in this research have unequivocally showcased the exceptional absorption capabilities of graphene-like film volumetric metasurfaces in the THz frequency range. The samples proposed and analyzed within this thesis stand out not only for their lightweight characteristics but also for their cost-effectiveness. Furthermore, the simplicity of their fabrication process underscores the viability and potential of 3D printing techniques in creating metasurfaces. This research paves the way for the broader adoption and development of 3D-printed metasurfaces, positioning them as leading candidates for perfect absorbers in future applications.

In our future research, we plan to utilize the same samples, extending our measurements to various angles of incidence. This approach will provide a comprehensive understanding of the angular dependence of the samples' optical properties. Doing so aims to gain deeper insights into their behaviour and performance, potentially unveiling novel phenomena and further optimizing their applications. We're getting ready to submit an article based on the outcomes of our recent study and expected studies. We aim to get our research published in one of the MDPI journals, either "Nanomaterials" or "Materials."

Reference

[1] E. Rutherford, “The structure of the atom,” *Phylosophical Mag.*, vol. 27, pp. 488–498, 2010.

[2] A. Erdemir and C. Donnet, “Tribology of diamond-like carbon films: Recent progress and future prospects,” *J. Phys. D. Appl. Phys.*, vol. 39, no. 18, Sep. 2006.

[3] A. H. Lettington, “Applications of diamond-like carbon thin films,” *Carbon N. Y.*, vol. 36, no. 5–6, pp. 555–560, 1998.

[4] “https://www.graphene-info.com/evd-graphene-prices-continue-drop-commercial-applications-start-enter-market.”

[5] L. Ju *et al.*, “Graphene plasmonics for tunable terahertz metamaterials,” *Nat. Nanotechnol.*, vol. 6, no. September, pp. 6–10, 2011.

[6] T. Kaplas and P. Kuzhir, “Ultra-thin graphitic film : synthesis and physical properties,” *Nanoscale Res. Lett.*, pp. 4–9, 2016.

[7] A. M. Lyons, L. P. Hale, and C. W. W. Jr, “Photodefinable carbon films : control of image quality,” *J. Vac. Sci. Technol. A*, vol. 1, no. 1985, pp. 447–452, 2015.

[8] M. Baah *et al.*, “Electrical , transport , and optical properties of multifunctional graphitic films synthesized on dielectric surfaces by nickel,” *Appl. Mater. interfaces*, vol. 12, pp. 6226–6233, 2020.

[9] L. Golubewa *et al.*, “All-optical thermometry with NV and SiV color centers in biocompatible diamond microneedles,” *Adv. Opt. Mater.*, vol. 10, p. 2200631, 2022.

[10] M. Baah *et al.*, “Electrical impedance sensing of organic pollutants with ultrathin graphitic membranes,” *Nanotechnology*, vol. 33, p. 075207, 2022.

[11] Q. Long *et al.*, “Electrochemical pyrolytic carbon resonators for mass sensing on electrodeposited polymers Publication date : Micro and Nano Engineering Electrochemical pyrolytic carbon resonators for mass sensing on electrodeposited polymers,” *Micro Nano Eng.*, vol. 2, pp. 64–69, 2019.

[12] A. A. Tseng, K. Chen, and C. D. Chen, “Electron beam lithography in nanoscale fabrication : Recent development,” *IEEE Trans. Electron. Packag. Manuf.*, vol. 26,

no. 2, pp. 141–149, 2003.

[13] I. B. Vendik and O. G. Vendik, “Metamaterials and their application in microwaves: A review,” *Tech. Phys.*, vol. 58, no. 1, pp. 1–24, 2013.

[14] N. Meinzer, W. L. Barnes, and I. R. Hooper, “Plasmonic meta-atoms and metasurfaces,” *Nat. Photonics*, vol. 8, no. 12, pp. 889–898, 2014.

[15] R. M. Walser, “Electromagnetic metamaterials. Complex Mediums II: beyond linear isotropic dielectrics,” *Int. Soc. Opt. Photonics*, vol. 4467, pp. 1–15, 2001.

[16] V. G. Veselago, “The Electrodynamic of Substances with Simultaneous Negative Values of Ɛ and μ,” *Sov. Phys. Uspekhi*, vol. 10, no. 4, pp. 509–514, 1968.

[17] C. H. Kodama and R. A. Coutu, “THz Metamaterial Characterization Using THz-TDS,” *Terahertz Spectrosc. - A Cut. Edge Technol.*, pp. 104–118, 2017.

[18] D. R. Smith, W. J. Padilla, D. C. Vier, N.-N. S. C., and S. S., “Composite medium with simultaneously negative permeability and permittivity,” *Phys. Rev. Lett.*, vol. 84, no. 18, pp. 4184–4187, 2015.

[19] N. Engheta, “Thin Absorbing Screens Using Metamaterial Surfaces,” *Antennas Propag. Soc. Int. Symp.*, vol. 2, pp. 392–395, 2002.

[20] N. I. Landy, S. Sajuyigbe, J. J. Mock, D. R. Smith, and W. J. Padilla, “Perfect metamaterial absorber,” *Phys. Rev. Lett.*, vol. 100, no. 20, pp. 1–4, 2008.

[21] A. Paddubskaya *et al.*, “Terahertz absorber with graphene enhanced polymer hemispheres array,” *Nanomaterials*, vol. 11, no. 10, pp. 0–7, 2021.

[22] Z. Yi *et al.*, “Graphene-based tunable triple-band plasmonic perfect metamaterial absorber with good angle-polarization-tolerance,” *Results Phys.*, vol. 13, no. 2, p. 102149, 2019.

[23] H. T. Chen, W. J. Padilla, J. M. O. Zide, A. C. Gossard, A. J. Taylor, and R. D. Averitt, “Active terahertz metamaterial devices,” *Nature*, vol. 444, no. 7119, pp. 597–600, 2006.

[24] X. C. Zhang, A. Shkurinov, and Y. Zhang, “Extreme terahertz science,” *Nat. Photonics*, vol. 11, no. 1, pp. 16–18, 2017.

[25] N. I. Zheludev and Y. S. Kivshar, “From metamaterials to metadevices,” *Nat. Mater.*, vol. 11, no. 11, pp. 917–924, 2012.

[26] L. D. Landau and E. M. Lifshitz, *Statistical physics*, vol. 44, no. 1127. 1916.

[27] J. M. Stillahn, K. J. Trevino, and E. R. Fisher, "Plasma diagnostics for unraveling process chemistry," *Annu. Rev. Anal. Chem.*, vol. 1, no. 1, pp. 261–291, 2008.

[28] Y. Wu, B. Yang, B. Zong, H. Sun, Z. Shen, and Y. Feng, "Carbon nanowalls and related materials," *J. Mater. Chem.*, vol. 14, pp. 469–477, 2004.

[29] H. W. Kroto, J. R. Heath, S. C. O'Brien, R. F. Curl, and R. E. Smalley, "C60: Buckminsterfullerene," *Nature*, vol. 318, no. 6042, pp. 162–163, 1985.

[30] S. Iijima, "Helical microtubules of graphitic carbon," *Nature*, vol. 354, pp. 56–58, 1991.

[31] "The History of Graphene - CealTech AS." https://cealtech.com/2017/05/09/the-history-of-graphene/ (accessed May 11, 2023).

[32] A. K. Geim and K. S. Novoselov, "The rise of graphene progress," *Nat. Mater.*, vol. 6, no. 3, pp. 183–191, 2007.

[33] K. S. Novoselov et al, "Electric field effect in atomically thin carbon films," vol. 306, pp. 666–669, 2016.

[34] K. I. Bolotin *et al.*, "Ultrahigh electron mobility in suspended graphene," *Solid State Commun.*, vol. 146, no. 9–10, pp. 351–355, 2008.

[35] A. S. Mayorov *et al.*, "Micrometer-scale ballistic transport in encapsulated graphene at room temperature," *Nano Lett.*, vol. 11, no. 6, pp. 2396–2399, 2011.

[36] J. Baringhaus *et al.*, "Exceptional ballistic transport in epitaxial graphene nanoribbons," *Nature*, vol. 506, no. 7488, pp. 349–354, 2014.

[37] M. I. Katsnelson, "Graphene: carbon in two dimensions," *Mater. Today*, vol. 10, no. 1–2, pp. 20–27, 2007.

[38] I. W. Frank, D. M. Tanenbaum, A. M. van der Zande, and P. L. McEuen, "Mechanical properties of suspended graphene sheets," *J. Vac. Sci. Technol. B Microelectron. Nanom. Struct.*, vol. 25, no. 6, p. 2558, 2007.

[39] C. Lee, X. Wei, J. W. Kysar, and J. Hone, "Measurement of the elastic properties and intrinsic strength of monolayer graphene," *Science (80-.).*, vol. 321, no. 5887, pp. 385–388, 2008.

[40] F. Liu, P. Ming, and J. Li, "Ab initio calculation of ideal strength and phonon

instability of graphene under tension," *Phys. Rev. B - Condens. Matter Mater. Phys.*, vol. 76, no. 6, pp. 1–7, 2007.

[41] R. J. Young, I. A. Kinloch, L. Gong, and K. S. Novoselov, "The mechanics of graphene nanocomposites: A review," *Compos. Sci. Technol.*, vol. 72, no. 12, pp. 1459–1476, 2012.

[42] L. Gong, I. A. Kinloch, R. J. Young, I. Riaz, R. Jalil, and K. S. Novoselov, "Interfacial stress transfer in a graphene monolayer nanocomposite," *Adv. Mater.*, vol. 22, no. 24, pp. 2694–2697, 2010.

[43] S. Bunch, J *et al.*, "Impermeable atomic membranes," *Nano Lett.*, vol. 8, no. 8, pp. 3–7, 2008.

[44] F. Schedin *et al.*, "Detection of individual gas molecules adsorbed on graphene," *Nat. Mater.*, vol. 6, no. 9, pp. 652–655, 2007.

[45] Z. H. Ni *et al.*, "Graphene thickness determination using reflection and contrast spectroscopy," *Nano Lett.*, vol. 7, no. 9, pp. 2758–2763, 2007.

[46] R. R. Nair *et al.*, "Fine structure constant defines visual transparency of graphene," *Science (80-.).*, vol. 320, no. 5881, p. 1308, 2008.

[47] K. Mansour, M. J. Soileau, and E. W. Van Stryland, "Nonlinear optical properties of carbon-black suspensions (ink)," *J. Opt. Soc. Am. B*, vol. 9, no. 7, p. 1100, 1992.

[48] L. W. T. & A. Kost, "Optical limiting in C60 and C70.pdf," *Nature*, vol. 356. pp. 225–226, 1992.

[49] T. Hasan *et al.*, "Nanotube - Polymer composites for ultrafast photonics," *Adv. Mater.*, vol. 21, no. 38–39, pp. 3874–3899, 2009.

[50] F. Bonaccorso, Z. Sun, T. Hasan, and A. C. Ferrari, "Graphene photonics and optoelectronics," *Nat. Photonics*, vol. 4, no. 9, pp. 611–622, 2010, doi: 10.1038/nphoton.2010.186.

[51] J. Wang and W. J. Blau, "Inorganic and hybrid nanostructures for optical limiting," *J. Opt. A Pure Appl. Opt.*, vol. 11, no. 2, 2009.

[52] L. W. Tutt and T. F. Boggess, "A review of optical limiting mechanisms and devices using organics, fullerenes, semiconductors and other materials," *Prog. Quantum Electron.*, vol. 17, no. 4, pp. 299–338, 1993.

[53] A. A. Balandin *et al.*, "Superior thermal conductivity of single-layer graphene,"

Nano Lett., vol. 8, no. 3, pp. 902–907, 2008.

[54] S. Ghosh *et al.*, "Dimensional crossover of thermal transport in few-layer graphene," *Nat. Mater.*, vol. 9, no. 7, pp. 555–558, 2010.

[55] A. A. Balandin, "Thermal properties of graphene and nanostructured carbon materials," *Nat. Mater.*, vol. 10, no. 8, pp. 569–581, 2011.

[56] S. Bae *et al.*, "Roll-to-roll production of 30-inch graphene films for transparent electrodes," *Nat. Nanotechnol.*, vol. 5, no. 8, pp. 574–578, 2010.

[57] C. N. R. Rao, A. K. Sood, K. S. Subrahmanyam, and A. Govindaraj, "Graphene: The new two-dimensional nanomaterial," *Angew. Chemie - Int. Ed.*, vol. 48, no. 42, pp. 7752–7777, 2009.

[58] X. Zhang, B. R. S. Rajaraman, H. Liu, and S. Ramakrishna, "Graphene's potential in materials science and engineering," *RSC Adv.*, vol. 4, no. 55, pp. 28987–29011, 2014.

[59] K. S. Novoselov *et al.*, "Electric field effect in atomically thin carbon films," *Science*, vol. 306, no. 5696, pp. 666–669, 2004.

[60] S. Kumar, N. Kaur, A. K. Sharma, A. Mahajan, and R. K. Bedi, "Improved Cl2 sensing characteristics of reduced graphene oxide when decorated with copper phthalocyanine nanoflowers," *RSC Adv.*, vol. 7, no. 41, pp. 25229–25236, 2017.

[61] G. Russakoff, "A derivation of the macroscopic Maxwell equations," *Am. J. Phys.*, vol. 38, no. 10, pp. 1188–1195, 1970.

[62] J. D. Jackson, *Classical electrodynamics*. 1962.

[63] L. D. Landau and E. M. Lifshitz, *Electrodynamics of Contunuous Media -Volume 8 of Theoretical Physics*. 1984.

[64] R. E. Raab and O. L. De Lange, "Multipole theory in electromagnetism : classical, quantum, and symmetry aspects, with applications," p. 235, 2005.

[65] R. F. Harrington, *Time-harmonic electromagnetic fields*. 2001.

[66] R. Alaee, C. Rockstuhl, and I. Fernandez-corbaton, "An electromagnetic multipole expansion beyond the long-wavelength approximation," *Opt. Commun.*, vol. 407, no. August 2017, pp. 17–21, 2018.

[67] A. Accelerator, "Multipole expansion." https://academic-

accelerator.com/encyclopedia/multipole-expansion

[68] N. I. Zheludev, S. A. Maier, N. J. Halas, P. Nordlander, H. Giessen, and C. T. Chong, "The Fano resonance in plasmonic nanostructures and metamaterials," *Nat. Publ. Gr.*, vol. 9, no. 9, pp. 707–715, 2010.

[69] S. Chiam, R. Singh, C. Rockstuhl, F. Lederer, W. Zhang, and A. A. Bettiol, "Analogue of electromagnetically induced transparency in a terahertz metamaterial," vol. 80, no. 4, p. 152103, 2009.

[70] Y. H. Fu, A. I. Kuznetsov, A. E. Miroshnichenko, Y. F. Yu, and B. Luk'yanchuk, "Directional visible light scattering by silicon nanoparticles," *Nat. Commun.*, vol. 4, pp. 1–6, 2013.

[71] L. Rogobete, F. Kaminski, M. Agio, and V. Sandoghdar, "Design of plasmonic nanoantennae for enhancing spontaneous emission," *Opt. Lett.*, vol. 32, no. 12, p. 1623, 2007.

[72] A. Alù and N. Engheta, "Multifrequency optical invisibility cloak with layered plasmonic shells," *Phys. Rev. Lett.*, vol. 100, no. 11, pp. 1–4, 2008.

[73] J. P. Barton, D. R. Alexander, and S. A. Schaub, "Theoretical determination of net radiation force and torque for a spherical particle illuminated by a focused laser beam," *J. Appl. Phys.*, vol. 66, no. 10, pp. 4594–4602, 1989.

[74] R. Alaee, C. Rockstuhl, and I. Fernandez-Corbaton, "An electromagnetic multipole expansion beyond the long-wavelength approximation," *Opt. Commun.*, vol. 407, no. May 2017, pp. 17–21, 2018.

[75] B. Lukyanchuk, R. Paniagua-Domínguez, A. I. Kuznetsov, A. E. Miroshnichenko, and Y. S. Kivshar, "Suppression of scattering for small dielectric particles: anapole mode and invisibility," *Philos. Trans. R. Soc. A Math. Phys. Eng. Sci.*, vol. 375, no. 2090, 2017.

[76] D. Smirnova and Y. S. Kivshar, "Multipolar nonlinear nanophotonics," *Optica*, vol. 3, no. 11, p. 1241, 2016.

[77] V. Savinov, N. Papasimakis, D. P. Tsai, and N. I. Zheludev, "Optical anapoles," *Commun. Phys.*, vol. 2, no. 1, pp. 10–13, 2019.

[78] N. Papasimakis, V. A. Fedotov, V. Savinov, T. A. Raybould, and N. I. Zheludev, "Electromagnetic toroidal excitations in matter and free space," *Nat. Mater.*, vol. 15, no. 3, pp. 263–271, 2016.

[79] K. Marinov, A. D. Boardman, V. A. Fedotov, and N. Zheludev, “Toroidal metamaterial,” *New J. Phys.*, vol. 9, no. 324, pp. 1–12, 2007.

[80] T. Kaelberer, V. A. Fedotov, N. Papasimakis, D. P. Tsai, and N. I. Zheludev, “Toroidal dipolar response in a metamaterial,” *Science (80-.).*, vol. 330, no. 6010, pp. 1510–1512, 2010.

[81] V. Savinov, V. A. Fedotov, and N. I. Zheludev, “Toroidal dipolar excitation and macroscopic electromagnetic properties of metamaterials,” *Phys. Rev. B - Condens. Matter Mater. Phys.*, vol. 89, no. 20, p. 205112, 2014.

[82] Y.-W. Huang *et al.*, “Design of plasmonic toroidal metamaterials at optical frequencies,” *Opt. Express*, vol. 20, no. 2, p. 1760, 2012.

[83] A. A. Basharin *et al.*, “Dielectric metamaterials with toroidal dipolar response,” *Phys. Rev. X*, vol. 5, no. 1, pp. 1–11, 2015.

[84] T. A. Raybould *et al.*, “Toroidal circular dichroism,” *Phys. Rev. B*, vol. 94, no. 3, pp. 2–6, 2016.

[85] Y. W. Huang, W. T. Chen, P. C. Wu, V. A. Fedotov, N. I. Zheludev, and D. P. Tsai, “Toroidal lasing spaser,” *Sci. Rep.*, vol. 3, pp. 1–4, 2013.

[86] M. Gupta, Y. K. Srivastava, M. Manjappa, and R. Singh, “Sensing with toroidal metamaterial,” *Appl. Phys. Lett.*, vol. 110, no. 12, p. 121108, 2017.

[87] N. Talebi, S. Guo, and P. A. Van Aken, “Theory and applications of toroidal moments in electrodynamics: Their emergence, characteristics, and technological relevance,” *Nanophotonics*, vol. 7, no. 1, pp. 93–110, 2018.

[88] N. A. Spaldin, M. Fiebig, and M. Mostovoy, “The toroidal moment in condensed-matter physics and its relation to the magnetoelectric effect,” *J. Phys. Condens. Matter*, vol. 20, p. 434303, 2008.

[89] Y. Gao, C. M. Ho, and R. J. Scherrer, “Anapole dark matter at the LHC,” *Phys. Rev. D - Part. Fields, Gravit. Cosmol.*, vol. 89, no. 4, pp. 1–5, 2014.

[90] S. Q. Li and K. B. Crozier, “Origin of the anapole condition as revealed by a simple expansion beyond the toroidal multipole,” *Phys. Rev. B*, vol. 97, no. 24, pp. 1–7, 2018.

[91] V. A. Fedotov, A. V. Rogacheva, V. Savinov, D. P. Tsai, and N. I. Zheludev, “Resonant transparency and non-trivial non-radiating excitations in toroidal metamaterials,” *Sci. Rep.*, vol. 3, pp. 1–5, 2013.

[92] A. E. Miroshnichenko *et al.*, "Nonradiating anapole modes in dielectric nanoparticles," *Nat. Commun.*, vol. 6, pp. 1–8, 2015.

[93] A. A. Basharin, V. Chuguevsky, N. Volsky, M. Kafesaki, and E. N. Economou, "Extremely high Q -factor metamaterials due to anapole excitation," *Phys. Rev. B*, vol. 95, no. 3, pp. 1–10, 2017.

[94] P. C. Wu *et al.*, "Optical Anapole Metamaterial," *ACS Nano*, vol. 12, no. 2, pp. 1920–1927, 2018.

[95] M. Kerker, D. Wang, and C. L. Giles, "Electromagnetic scattering by magnetic spheres," *J. Opt. Soc. Am.*, vol. 73, no. 6, pp. 765–767, 1983.

[96] G. Raquel *et al.*, "Electric and magnetic dipolar response of germanium nanospheres : interference effects , scattering anisotropy , and optical forces," *J. Nanophotonics*, vol. 5, p. 053512, 2011.

[97] J. P. Connerade and A. M. Lane, "Interacting resonances in atomic spectroscopy," *Reports Prog. Phys.*, vol. 51, no. 11, pp. 1439–1478, 1988.

[98] M. F. Limonov, M. V. Rybin, A. N. Poddubny, and Y. S. Kivshar, "Fano resonances in photonics," *Nat. Photonics*, vol. 11, no. 9, pp. 543–554, 2017.

[99] E. Hola *et al.*, "New bimolecular photoinitiating systems based on terphenyl derivatives as highly efficient photosensitizers for 3D printing application," *Polym. Chem.*, vol. 11, no. 4, pp. 922–935, 2020.

[100] P. Martin, "Analysing LCD display colour masks using transmission microspectroscopy.," *Craic Technol.*, vol. 1, pp. 1–8, 2008.

[101] H. Quan, T. Zhang, H. Xu, S. Luo, J. Nie, and X. Zhu, "Photo-curing 3D printing technique and its challenges," *Bioact. Mater.*, vol. 5, no. 1, pp. 110–115, 2020.

[102] T. Kaplas, A. Matikainen, T. Nuutinen, S. Suvanto, and P. Vahimaa, "Scalable fabrication of the graphitic substrates for graphene-enhanced Raman spectroscopy," *Sci. Rep.*, vol. 7, pp. 1–6, 2017.

[103] N. Pyrolysis *et al.*, "Electrical , transport , and optical properties of multifunctional graphitic Films synthesized on dielectric surfaces by nickel," *Appl. Mater. interfaces*, vol. 12, pp. 6226–6233, 2020.

[104] M. Schreiber *et al.*, "Applied surface science transparent ultrathin conducting carbon films," *Appl. Surf. Sci.*, vol. 256, no. 21, pp. 6186–6190, 2010.

[105] M. Karabiyik, C. Al-amin, and N. Pala, “Graphene-based periodic gate field effect transistor structures for terahertz applications,” vol. 5, no. 7, pp. 754–757, 2013.

[106] I. Ivanov, M. Bonn, Z. Mics, and D. Turchinovich, “Perspective on terahertz spectroscopy of graphene,” *Europhys. Lett.*, vol. 111, no. 6, p. 67001, 2015.

List of Symbols, Operators and Special functions

Symbols

A	vector potential
B	magnetic flux density
C_{a}	scattering cross-section
C_{s}	electric dipole scattering cross section
C_s^m	magnetic dipole scattering cross section
e^q	electric quadrupole scattering cross section
D	electric displacement
E	electric field
H	magnetic field
$\mathbf{J}$	macroscopic current density
$\mathbf{J}_{\mathrm{c.e}}$	spatially averaged conduction electron current density
$\mathbf{J}_F$	free current density

Operators

.	dot product
$\times$	cross product
∇	nabla operator
$\mathrm{Re}\{a\}$	real part of a
$\mathrm{Im}\{a\}$	imaginary part of a
$\frac{\mathrm{d}}{\mathrm{d}t}$	Differentiation with respect to t
$\sum$	summation

Special functions

j_l	spherical Bessel function of order l
$\delta(x)$	one-dimensional Dirac delta function
$\delta(\mathbf{r}-\mathbf{r}')$	three-dimensional Dirac delta function $=\delta(x-x')\delta(y-y')\delta(z-z')$
$\delta(\mathbf{r})$	three-dimensional Dirac delta function at origin $=\delta(r)/(4\pi r^2)$

M	magnetization
P	electric polarization
$\overleftrightarrow{Q}$	electric quadrupole moment density
$\overleftrightarrow{Q}$	current quadrupole moment
b	microscopic magnetic flux density
c	speed of light in vacuum $=$ $299{,}792{,}458\ \mathrm{ms}^{-1}$
e	microscopic electric field
$\mathbf{j}_m$	microscopic current density
k	wave number $= 2\pi\lambda^{-1}$
$\mathbf{k}$	wave vector
P	electric dipole moment
m	magnetic dipole moment
q	electric charge
$\mathbf{r}$	position
t	time
ϵ_0	electric permittivity in vacuum $= \mu_0^{-1}c^{-2}$
μ_0	magnetic permeability in vacuum $= 4\pi \times 10^{-7}\mathrm{Nm}^{-2}$

ρ	macroscopic charge density
ρ_F	free charge density
ρ_m	microscopic charge density
ω	angular frequency

Personal Statement of Non-plagiarism

I, Muhammad Muaz Iqbal, hereby declare that all information in this report has been obtained and presented in accordance with academic rules and ethical conduct, and the work I am submitting in this report, except where I have indicated, is my own work**.**

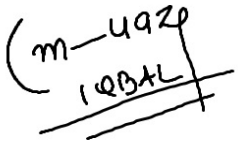

Muhammad Muaz Iqbal

22 August 2023

Supervisor Approval

I, the undersigned, **Polina Kuzhir**, supervisor of [Muhammad Muaz Iqbal], student of the PSRS EMJMD, during his master thesis at **University of Eastern Finland** certify that I approve the content of this master thesis report entitled Graphene- enhanced dielectric metasurface: toward close to perfect absorption.

Date and signature of the supervisor

Polina Kuzhir

Joensuu, 22, August, 2023

Right and Permission

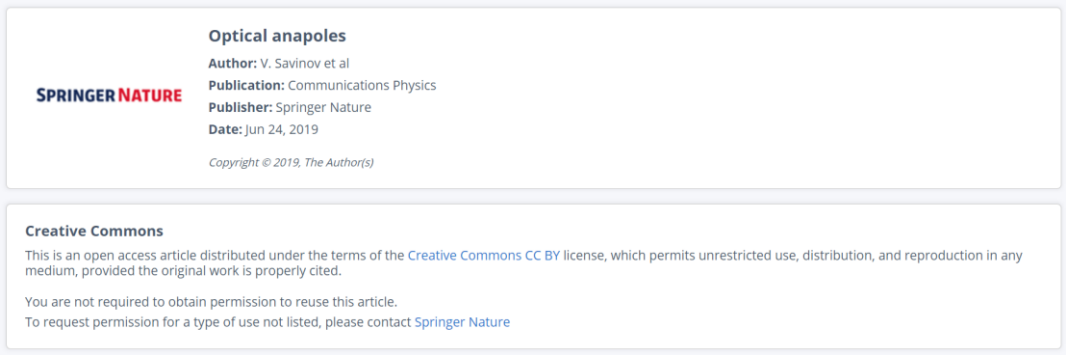

SPRINGER NATURE

Optical anapoles

Author: V. Savinov et al
Publication: Communications Physics
Publisher: Springer Nature
Date: Jun 24, 2019

Copyright © 2019, The Author(s)

Creative Commons

This is an open access article distributed under the terms of the Creative Commons CC BY license, which permits unrestricted use, distribution, and reproduction in any medium, provided the original work is properly cited.

You are not required to obtain permission to reuse this article.
To request permission for a type of use not listed, please contact Springer Nature